International Journal of Material Forming (2022) 15: 8
https://doi.org/10.1007/s12289-022-01655-x

DEVELOPMENTS IN MODELLING AND SIMULATION..JAPAN, SOUTH KOREA AND CHINA

Cylindrical cup drawing of a commercially pure titanium sheet: experiment and crystal plasticity finite-element simulation

Takayuki Hama[1] · **Kaho Hirano**[1] · **Ryo Matsuura**[1]

Received: 23 June 2021 / Accepted: 10 January 2022 / Published online: 1 February 2022

Abstract
Because of the strong anisotropy in mechanical properties, press forming of commercially pure titanium (CP-Ti) sheets often creates significant defects, including earing formation during drawing. However, the predictive accuracy of CP-Ti sheet drawing processes by finite-element simulations is still not satisfactory because it is difficult to accurately represent the strong anisotropy with phenomenological constitutive models. In this study, a crystal plasticity model is employed to conduct finite-element simulations of a cold-rolled Grade 2 CP-Ti sheet cup drawing process, and its applicability to the process is examined in detail by comparing it with experimental results. Experimentally, the maximum cup height appears at an angle of approximately 50° from the rolling direction, and the heights at 0° and 90° are similar. The thickness strain distribution evolution is strongly dependent on the direction. Twinning activity during drawing is the largest at 90°, followed by 45°, and then 0°. The simulation qualitatively captures the overall tendencies well, but non-negligible discrepancies are also involved in the cup height at 90°, and the thickening at the cup edge at 0° and 90°. The mechanisms that yield the discrepancies between the experiment and the simulation are examined. Moreover, parametric studies are conducted to discuss the effects of twinning activity and friction on the drawability.

Keywords Commercially pure titanium sheet · Cup drawing · Crystal plasticity · Finite-element method · Twinning · Earing

Introduction

Commercially pure titanium (CP-Ti) has prominent properties, such as high specific strength, corrosion resistance, burning resistance, and biocompatibility, and has been widely used in industrial applications, such as in automobiles [1] and biomedical components [2].

CP-Ti sheets exhibit strong anisotropy and numerous studies have investigated the anisotropic deformation behavior of CP-Ti sheets [for example, 3–14]. Baral et al. [14] conducted uniaxial tension, uniaxial compression, and plane-strain tension of a Grade 2 CP-Ti sheet and demonstrated that the sheet exhibited in-plane anisotropies in the stress–strain curves and Lankford values (r-value) under uniaxial tension. Furthermore, they also showed that the evolution of the in-plane anisotropy of the flow stress differed between tension and compression. Bouvier et al. [9] conducted simple shear tests on high-purity α-Ti sheets and showed that the in-plane anisotropy of the hardening behavior appeared under monotonic, reverse, and cyclic loadings. Under monotonic loading, the anisotropy was initially low, whereas it became more pronounced with an increasing shear strain. Hama et al. [11] and Yi et al. [12] performed reverse loadings of CP-Ti sheets and showed that a sigmoidal work-hardening curve appeared during tension following compression, as in magnesium alloy sheets.

The strong anisotropy observed in CP-Ti sheets primarily results from the rolling texture with the c-axes tilted at approximately 30° from the normal direction (ND) toward the transverse direction (TD) [4, 5, 7, 10]. Additionally, CP-Ti sheets exhibit strong crystal anisotropy of the hexagonal close-packed (hcp) structure at room temperature, which also causes the strongly anisotropic plastic

This article is part of the Topical Collection on *Liver*

✉ Takayuki Hama
hama@energy.kyoto-u.ac.jp

[1] Graduate School of Energy Science, Kyoto University, Yoshida-honmachi, Sakyo-ku, Kyoto 606-8501, Japan

deformation behavior. The crystalline anisotropy in the hcp structure occurs because of the differences in critical resolved shear stress (CRSS) and work hardening which depend on slip and twinning systems. At room temperature, the primary slip systems are prismatic < a > slip, and the basal < a > and pyramidal < a > slip systems are also active [11, 12, 15–23]. It is difficult for these slip systems to contribute to the through-thickness plastic deformation of rolled CP-Ti sheets because of the basal texture. Therefore, in addition to these < a > slip systems, the activities of pyramidal < a + c > slip or twinning systems are required [4, 7, 17, 18, 23–30]. It has been reported that $\{10\bar{1}2\}$ extension twinning and $\{11\bar{2}2\}$ contraction twinning systems are active at room temperature during the plastic deformation of CP-Ti sheets [11–13, 18].

CP-Ti sheets are often subjected to press forming processes to manufacture thin-walled components [31–33]. During press forming, sheets often undergo complicated deformations, including cyclic loadings, such as bending-unbending, and multiaxial loadings. For instance, during cylindrical cup drawing processes, material points at the flange part of the sheet are subjected to compressive deformation in the circumferential direction at the beginning of drawing. As the material points are drawn into the die cavity, they simultaneously undergo bending-unbending in the radial direction at the die shoulder [34]. Consequent to the complicated deformations, drawn cups often exhibit significant earing. Because earing in CP-Ti sheets tends to be pronounced because of the strong anisotropy, it is important to understand the anisotropic mechanical properties and drawability of CP-Ti sheets to enhance the industrial applications of CP-Ti sheets [35].

To this end, numerous experimental and numerical studies have been conducted to understand the cup drawability of rolled CP-Ti sheets [31–33, 35–45]. Kuwabara et al. [31] conducted cup drawing of a Grade 1 CP-Ti sheet and reported that the observed ear position was approximately 37° from the rolling direction (RD). Moreover, they simulated cup drawing using PAM-STAMP with Hill's quadratic [46] and non-quadratic [47] yield functions, and compared the results with experimental results. Ohwue et al. [44] conducted a circular-shell deep-drawing test of a Grade 1 CP-Ti sheet and a finite-element method (FEM) simulation utilizing LS-DYNA with the Barlat-Lian anisotropic yield function [48] to investigate the generation of earing. Raemy et al. [35] performed cup-drawing simulations of a Grade 4 CP-Ti sheet utilizing five constitutive models, including those proposed by von Mises [49], Hill [46], Cazacu et al. [50], Plunkett et al. [51], and the Fourier asymmetric yield model [35]. They then compared the simulation and experimental results of the thickness strain and punch force to verify the simulation.

Although some simulations in the aforementioned studies predicted the qualitative trends observed in the experiments well, further improvements are still necessary. One of the reasons for the low predictive accuracy is the evolution of anisotropy. In the aforementioned studies, different yield functions were used to represent the deformation behavior of the CP-Ti sheets. In CP-Ti sheets, anisotropic properties, including *r*-values and equal plastic work contour, usually evolve as the plastic deformation proceeds. Therefore, it is vital to consider the evolution of anisotropic properties for accurate material modeling. However, it has often been neglected but is considered to remain unchanged. This simplified material modeling could lead to a low predictive accuracy for press formability.

As an alternative approach of material modeling, crystal plasticity models are useful for describing the plastic deformations of various metals, and in recent years, they have been extensively used for CP-Ti sheets [52–68]. Hama et al. [62] proposed a crystal plasticity model for CP-Ti sheets and showed that the model accurately represented the plastic deformation of a Grade 1 CP-Ti sheet, including the stress–strain curves under tension, compression, and reverse loading along different in-plane directions, the evolution of *r*-values, and the anisotropic hardening of equal plastic work contour. Wronski et al. [63] proposed a twin variant selection criterion using a Monte Carlo approach within a viscoplastic self-consistent model and showed that the proposed model captured the activation of the low Schmid factor variants observed experimentally. Ma et al. [65] used a self-consistent crystal plasticity model that incorporated an enhanced twinning model to reproduce work-hardening behaviors under various loading conditions of Grade 1 and 2 CP-Ti sheets. Xiong et al. [68] conducted in-situ X-ray diffraction measurements and crystal plasticity simulations to characterize the time-dependent plastic deformation behavior of a Grade 4 CP-Ti sample. They found that prismatic slip exhibited a stronger strain rate sensitivity than basal slip at low strain rates, which significantly affected the stress redistribution to hard grain orientations.

The abovementioned recent achievements in crystal plasticity modeling for CP-Ti sheets suggest that the drawability of CP-Ti sheets can be predicted well by using crystal plasticity models. To date, crystal plasticity models have been utilized in finite-element simulations of cup drawing processes in various sheet metals [69–76]. Nakamachi et al. [69] conducted elastic/crystalline viscoplastic finite-element simulations of the cylindrical cup deep drawing processes of steel sheets. The strain localization and earing formation simulation results agreed well with the experimental results. The simulation results showed that the crystal orientation fibers correlated with the occurrence of failure and earing. Shi et al. [73] developed a crystal plasticity FEM to simulate the drawing process of an AA3014-H19 aluminum

sheet. The simulation results showed that the spatial distributions of the texture components, as well as the initial texture, played important roles in earing. Moreover, it was suggested that the earing type was dependent on the texture band formed in the sheet. Barrett et al. [75] conducted a finite-element simulation of the hemispherical cup drawing of a rolled-uranium sheet using an elastoplastic self-consistent crystal plasticity model and showed that the texture evolution at different points was reproduced well. Feng et al. [76] used an elastoplastic self-consistent crystal plasticity model to conduct finite-element simulations of a cylindrical cup deep drawing process for an AA6022-T4 sheet. The simulation results predicted the cup height, cup thinning, and force–displacement curve with acceptable accuracy. Moreover, the predictive accuracy and computational efficiency of the simulation was compared with that obtained with an anisotropic yield function and distortional hardening.

These studies demonstrate that crystal plasticity models can improve and enhance finite-element simulations of drawing processes. However, applications of crystal plasticity models to the deep drawing processes of CP-Ti sheets are scarce.

In this study, crystal plasticity finite-element simulations and experiments of a cylindrical cup drawing process with a CP-Ti sheet were conducted, and the applicability of the crystal plasticity model to the forming process simulation of a CP-Ti sheet is discussed. First, cup drawing experiments were performed and the cup geometries, including the earing profile and thickness distributions, and texture evolution were examined. A crystal plasticity finite-element simulation of the cup drawing process was then conducted, and the simulation results were rigorously compared with the experimental results. The deformation mechanism during cup drawing is also discussed using the simulation results. Furthermore, parametric studies were conducted to discuss the effects of twinning activity and friction on the drawability.

Experimental procedure

Material

The material used in this study was a 1.0 mm-thick cold-rolled Grade 2 CP-Ti sheet produced by Nippon Steel & Sumitomo Metal Co. The sheet was annealed for 1 h at 530 °C before testing. Table 1 lists the tensile properties along the RD, TD, and diagonal direction (45D).

Table 1 Mechanical properties of the CP-Ti sheet used in this study

	RD	45D	TD
E(GPa)	104	105	117
$\sigma_{0.2}$(MPa)	222	258	282
σ_T(MPa)	407	349	359
A_u(%)	17.8	11.2	7.9

*E: Young's modulus, $\sigma_{0.2}$: 0.2% prrof stress

σ_T: Tensile strengh, A_u: Uniform elongation

Cylindrical cup drawing

Figure 1 presents a photograph of the cylindrical cup drawing experimental setup. The punch diameter and punch shoulder radius were set to 27.8 mm and 5.0 mm, respectively. The die cavity diameter and the die shoulder radius were 30.0 mm and 7.0 mm, respectively; therefore, the clearance between the die and the punch was 1.1 mm. The diameter of the circular-shaped blank was 50.0 mm, corresponding to a drawing ratio of 1.67. The blank holding forces were determined using four springs. The distance between the die and the blank holder was kept constant at 1.1 mm during forming by using shims. The stroke speed was set to 5.0 mm/min. A solid lubricant (Moly Paste, Sumico Lubricant Co.) was used for lubrication. It should be noted that galling between the sheet and tool materials, which is sometimes problematic in the forming of CP-Ti sheets [77], did not occur in this study.

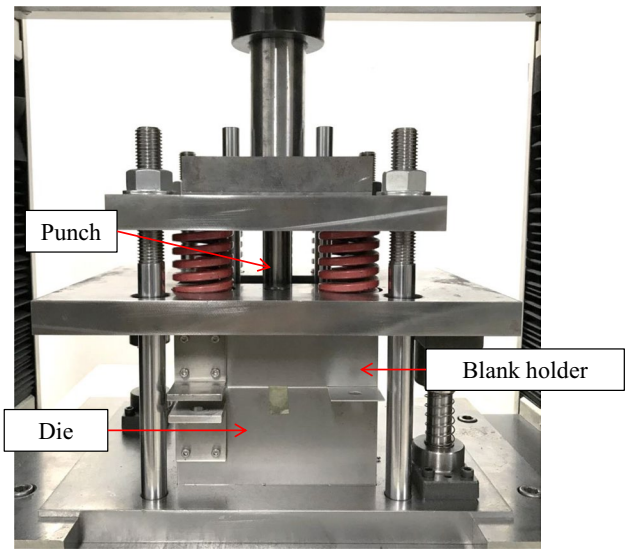

Fig. 1 Experimental setup for the cylindrical cup drawing

The earing profiles of the drawn cups were measured using a two-dimensional laser displacement sensor (LJ-V7080, Keyence Co.). Figure 2 defines the x–y-z coordinate system where the x, y, and z directions correspond to the RD, cup height, and TD, respectively. Geometries in the x–y plane were measured at every 0.05 mm in the z direction. The resolutions of the measurement were 0.024 mm and 0.5 µm for the x and y directions, respectively. Moreover, a

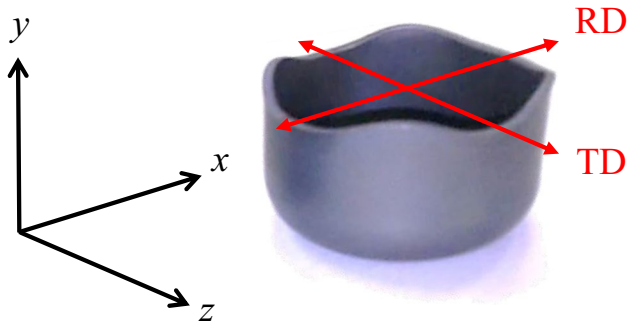

Fig. 2 Geometrical measurement of the drawn cup

micrometer (CPM15-25DM, Mitutoyo Co.) measured the thickness distributions of the drawn cups. The thickness was measured at every 1.0 mm in the radial direction along the RD, TD, and 45D.

The measurements were performed on three samples to confirm the reproducibility, and the average was reported.

Measurement of microstructures

Electron backscattered diffraction (EBSD) was used to measure the microstructures before and after cup drawing. Measurements were performed with a step size of 0.25 μm for all conditions. The OIM-Analysis 7 software (TSL Solutions) was used to obtain pole figures and inverse pole figure (IPF) maps. Only data with a confidence index larger than 0.1 were utilized for the analyses.

Figure 3a shows the initial experimentally measured pole figures. The typical rolling texture of CP-Ti sheets with basal planes tilted around 30° from the ND toward the TD was observed. The average grain diameter was approximately 17 μm.

The microstructures of the drawn cups were measured at six positions on the cup edge, as shown schematically in Fig. 4. Specifically, measurements were conducted along the RD, TD, and 45D for two positions near the inner and outer surfaces. The cup edge was polished before the measurements were performed.

Crystal plasticity FEM

Crystal plasticity model

The crystal plasticity FEM used in this study followed that used in our previous studies [62, 78]; therefore, the reader is referred to the aforementioned literature for the detailed formulations. The activity of each slip system was presumed to follow the Schmid's law. The following viscoplastic

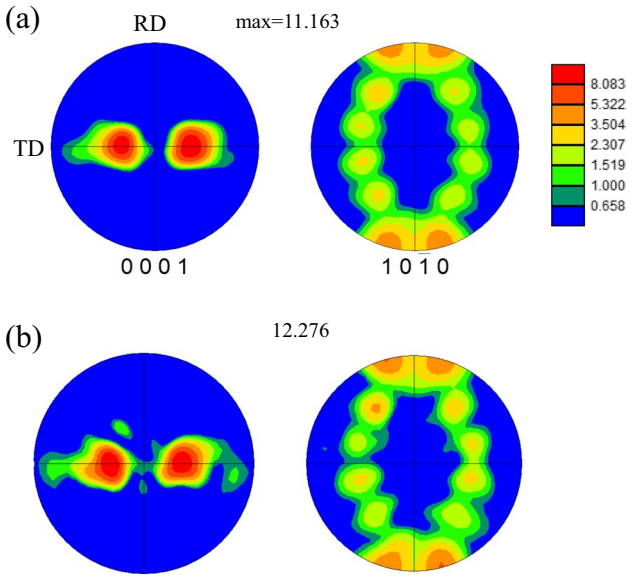

Fig. 3 Pole figures of the initial sample. a EBSD measurement results and b results obtained from the 400 orientations assigned to the simulation model

power law is used to represent the slip rate, $\dot{\gamma}^{(\alpha)}$, of the α -slip system:

$$\frac{\dot{\gamma}^{(\alpha)}}{\dot{\gamma}_0} = \left|\frac{\tau^{(\alpha)}}{\tau_Y^{(\alpha)}}\right|^{\frac{1}{m}} \mathrm{sign}\left(\tau^{(\alpha)}\right), \dot{\tau_Y}^{(\alpha)} = \sum_{\beta} q_{\alpha\beta} h \left|\dot{\gamma}^{(\beta)}\right| \tag{1}$$

$$\tau^{(\alpha)} = \boldsymbol{s}^{(\alpha)} \bullet \boldsymbol{\sigma} \bullet \boldsymbol{m}^{(\alpha)} \tag{2}$$

where $\tau^{(\alpha)}$ is the resolved shear stress, $\tau_Y^{(\alpha)}$ is the current strength of the α-slip system whose initial value is the CRSS, τ_0. $\dot{\gamma}_0$ is the reference strain rate, $q_{\alpha\beta}$ is the self ($\alpha = \beta$) and latent ($\alpha \neq \beta$) hardening moduli, and m is the rate-sensitivity exponent. The unit vectors $\boldsymbol{s}^{(\alpha)}$ and $\boldsymbol{m}^{(\alpha)}$ denote the slip direction and the normal to the slip plane, respectively. Five families of slip systems, namely basal < a > slip, prismatic < a > slip, pyramidal < a > slip, pyramidal < a + c > -1 slip, and pyramidal < a + c > -2 slip, and two families of twinning systems, namely $\{10\bar{1}2\}$ extension twinning and $\{11\bar{2}2\}$ contraction twinning, were considered. The following two equations were used for the rate of hardening, h:

$$h = h_0 \tag{3}$$

$$h = h_0\left(1 - \frac{\tau_0}{\tau_\infty}\right)\exp\left(-\frac{h_0\bar{\gamma}}{\tau_\infty}\right) \tag{4}$$

where $\bar{\gamma}$ is the cumulative slip rate of all slip systems, which is given in the form:

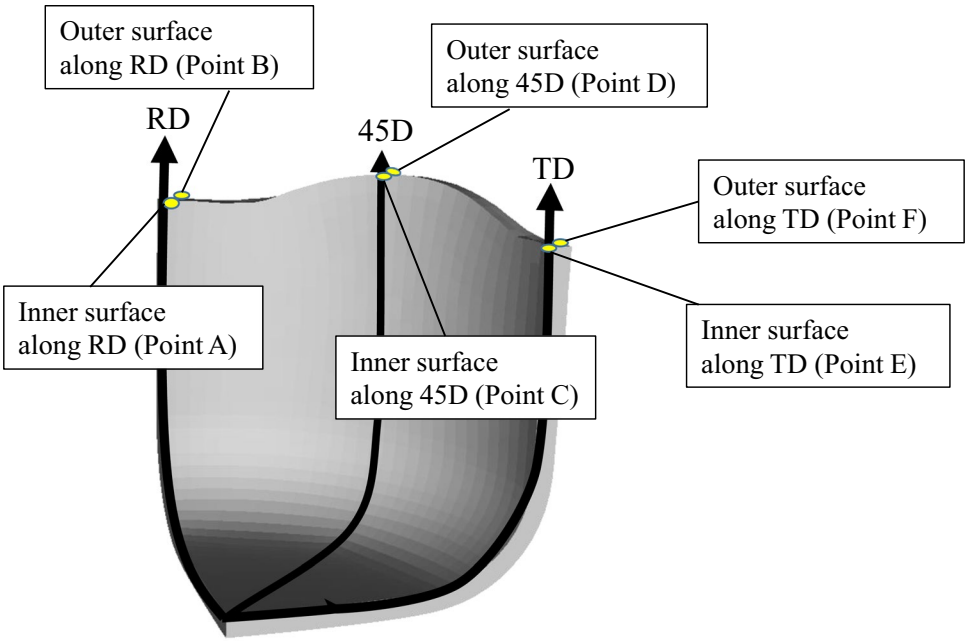

Fig. 4 Example of an EBSD measurement area

$$\overline{\gamma} = \sum_{\alpha} \int \left| \dot{\gamma}^{(\alpha)} \right| \mathrm{d}t \tag{5}$$

Linear hardening (Eq. (3)) was used for the twinning systems, whereas the Voce hardening (Eq. (4)) was assumed for the slip systems. The model proposed in a previous study [62] was used to describe twinning and detwinning. The determination of the material parameters used in Eqs. (1), (3), and (4) are explained below.

The crystal plasticity model was implemented into a FEM program, where explicit time integration was utilized [78]. The explicit time integration scheme was used to avoid numerical instabilities, especially arising from contact between tools and material [79–81]. In contrast, one of the disadvantages of this scheme is that rigorous equilibrium between internal and external forces is not guaranteed [81]. Therefore, to avoid excessive increases in non-equilibrated forces, the $r_{\min}$ method [82] was used. In the $r_{\min}$ method, the increments of various variables, for example, stress, strain, rotation, and slip increment, are monitored in each step. If the increments exceed prescribed admissible tolerances, the step size is limited so that the increments of all variables are always within the tolerances; thus, excessive increases in non-equilibrated forces can be avoided. Reader is referred to literatures [79–82] for details.

Simulation procedures

Finite-element model

Figure 5 shows the finite-element model used for the cup drawing simulations. Owing to the symmetry of the process, only one quarter of the cup was modeled. The x and z axes corresponded to the RD and TD, respectively, as

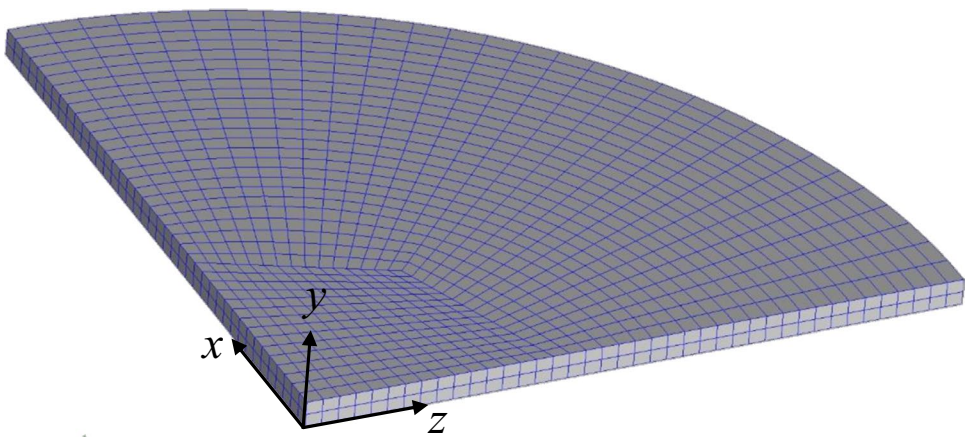

Fig. 5 Finite-element model used in the cup drawing simulation

shown in Fig. 2. Regarding boundary conditions, the displacements of the nodes on the $x=0$ and $z=0$ planes were fixed in the x and z directions, respectively, to represent the symmetries. To align with the experimental conditions, the thickness and diameter were set to 1.0 mm and 50.0 mm, respectively. An eight-node isoparametric brick element with selective reduced integration [83] was used for discretization. It should be noted that, due to limitations in mesh generation, the sheet was not discretized radially near the center, which may lead to poor predictive accuracies in this area [for example, 84, 85]. To minimize this effect, this area was made small as much as possible so that this area located only at the punch bottom whose deformation is small.

One-point quadrature elements have often been used for sheet metal forming simulations using crystal plasticity FEMs [72, 74, 76]. However, finite elements with eight integration points were employed in this study because bending and unbending are involved during forming; thus, it was important to evaluate the through-thickness stress and strain evolution. One-quarter of the sheet was divided into 1950 elements. Two layers were provided through the thickness. Four hundred crystal orientations were assigned to each integration point based on the Taylor model [86, 87]; thus, the model considered 6,240,000 orientations. Figure 3b shows the initial pole figures obtained from the 400 crystal orientations assigned to an integration point. The pole figures were obtained by using the OIM-Analysis 7 software, as in the case of the experimental result. They reproduced the experimental results shown in Fig. 3(a) well.

The numbers of finite elements and crystal orientations were determined as follows. In our previous study [62], the effect of the number of initial orientations on a stress–strain curve under uniaxial tension was examined for a Grade 1 CP-Ti sheet. It was shown that the stress–strain curve slightly depended on the set of initial orientations when 125 orientations were used, whereas it was almost independent of the set when 343 orientations were employed. These results suggested that 343 or larger orientations would be sufficient to reproduce the deformation behavior of CP-Ti sheets with strong basal texture; thus, the number of initial orientations was set to 400 in this study. Accordingly, the number of finite elements was set to 1950 considering the admissible calculation time. The effects of the numbers of initial orientations and finite elements on the cup drawing simulation are described in Appendix 1.

The tool geometries were similar to those of the experimental conditions. The tools were modeled as rigid, and their surfaces were represented by analytic functions. The Coulomb friction law was assumed between the sheet and tool surfaces. The friction coefficient was set to 0.1 to achieve a reasonable fit in the punch force–stroke curve between the experiment and simulation, as explained below.

Table 2 Identified material parameters for each slip and twinning system, in MPa

	CRSS(τ_0)	τ_∞	h_0
Basal	243	234	2337
Prism	59	192	1997
Pyr.<a>	91	151	695
Pyr.<a+c>-1	191	435	2456
Pyr.<a+c>-2	170	534	2456
$\{10\bar{1}2\}$twin	175	-	672
$\{11\bar{2}2\}$twin	211	-	672

Table 3 Latent-hardening parameters, $q_{\alpha\beta}$, used in simulations

	Basal Prism. Pyr.<a> Pyr._1 Pyr._2	$\{10\bar{1}2\}$	$\{11\bar{2}2\}$
Basal Prism. Pyr.<a> $\{10\bar{1}2\}$ $\{11\bar{2}2\}$	0.4	0.65	0.65
Pyr._1 Pyr._2	0.4	1.6	1.92

Parameter identification

The Young's modulus was set to $E=110$ GPa and Poisson's ratio was taken to be $\nu=0.3$. The reference strain rate was set to $\dot{\gamma}_0 = 0.001\ \mathrm{s}^{-1}$ and the rate sensitivity exponent was $m=0.02$. The self-hardening parameters of $q_{\alpha\beta}$ were set to unity.

The hardening parameters of the crystal plasticity model were determined as follows. To reproduce the stress–strain curves and the r-value evolution under uniaxial loadings in the RD, 45D and TD in each element of the finite-element model shown in Fig. 5, uniaxial loading simulations were performed using a single finite element with the 400 crystal orientations in each integration point. Determination procedures followed that reported in a previous study [62] and are explained in Appendix 2. Tables 2 and 3 list the hardening parameters used in this study. Figure 6 shows the simulation and experimental results of the stress–strain curves under tension and compression in the RD, 45D, and TD.

Under tension, the stress at yielding was the largest in the TD, while the stresses in the RD and the 45D were similar. In contrast, at large strains, the stress was the largest in the RD, followed in order by the TD and the 45D. Under compression, the stress in the TD was the largest, while the stresses

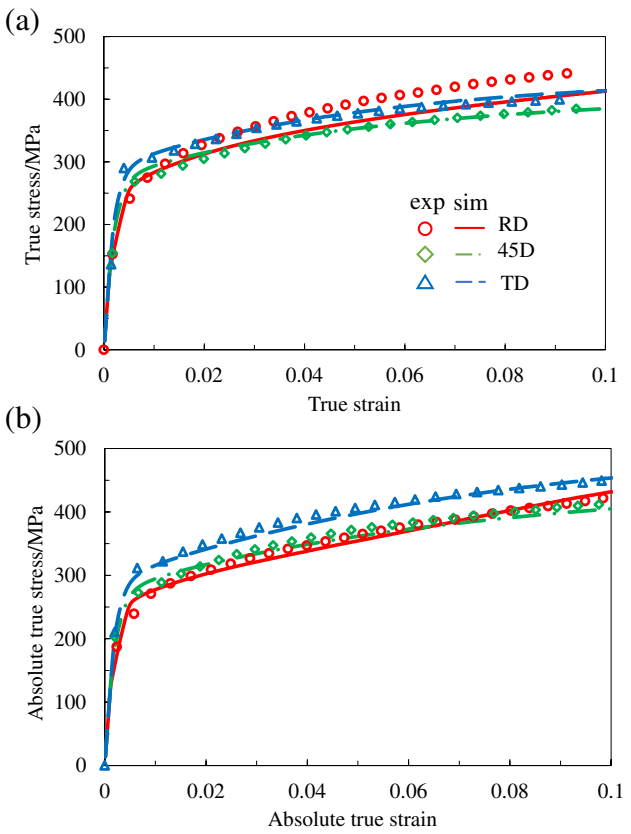

Fig. 6 Stress–strain curves obtained from the experiment and simulation under **a** tension and **b** compression

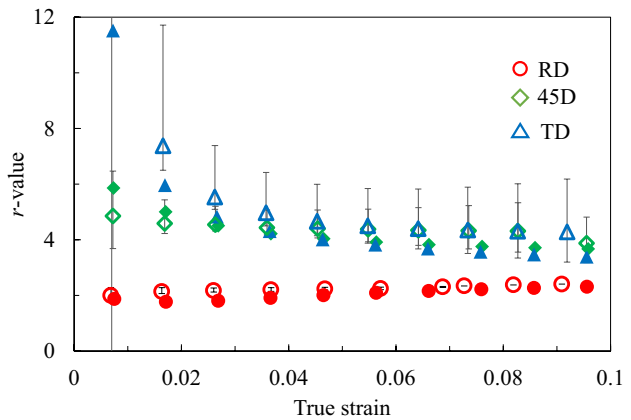

Fig. 7 Evolution of the r-value in the RD, 45D, and TD obtained from the experiment and simulation. Open and solid marks denote experimental and simulation results, respectively

in the RD and the 45D were similar. Obvious tension–compression asymmetry occurred, and moreover, the in-plane anisotropy differed between tension and compression.

Figure 7 shows the *r*-value evolution under tension in the RD, 45D, and TD. The *r*-value was initially the largest in the TD, followed in order by the 45D and the RD. The *r*-values in the TD and the 45D decreased as the strain increased, whereas the *r*-value remained almost unchanged in the RD. At large strains, the *r*-values in the TD and the 45D were similar and larger than the *r*-value in the RD. The results of the RD and the TD in Figs. 6 and 7 were qualitatively similar to those for a Grade 1 CP-Ti sheet reported in a previous study [62]. In the simulation results, although the stress level under RD tension was underestimated, the other simulation results of the stress–strain curves and the *r*-value evolution qualitatively agreed with the experimental results. Compared to the parameters determined for a Grade 1 CP-Ti sheet in a previous study [62], the magnitude relationship of CRSS between the deformation modes was slightly different. This difference may be due to the difference in the simulation procedure where a representative volume element consisting of multiple finite elements was utilized in the previous work, whereas the Taylor model was used in the present study. Another reason may be the differences in the material grades. The latent-hardening parameters were also slightly different from those determined in a previous study [62] to achieve better agreement for the present material.

It has been pointed out that contraction twinning in CP-Ti are affected by non-Schmid effects [88] and that non-Schmid effects play a role in tension–compression asymmetry in stress–strain curves [for example, 89, 90]. For instance, Sinha et al. [88] reported that contraction twinning with a low Schmid factor forms more easily than extension twinning with a high Schmid factor because of non-Schmid effects. Alleman et al. [91] reported that tension–compression asymmetry in stress–strain curve of single crystal tantalum resulted from the slip-direction dependency of the flow stress. These past studies suggested that, although the tension–compression asymmetry in the Grade 2 CP-Ti sheet was reproduced well without considering non-Schmid effects in this study, the parameter calibration as well as the predictive accuracy could be further improved by considering non-Schmid effects.

Results of cup drawing

Deformed geometry and punch force–stroke curve

Figure 8 shows the deformed shapes for the different strokes. It should be noted that the simulation results of the quarter part of the cup were mirror-copied to the other three quadrants to represent a full cup. The flange part of the sheet was detached from the upper surface of the die at a stroke of approximately 12 mm and was completely drawn into the die cavity at a stroke of approximately 21 mm. The sheet was completely drawn at a stroke of approximately 27 mm. Four ears appeared in both the experiment and the simulation.

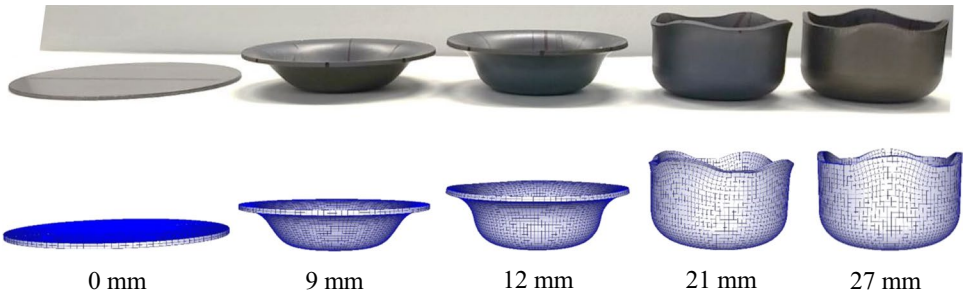

Fig. 8 Deformed shapes at the strokes of 0, 9, 12, 21, and 27 mm. The upper photographs are experimental results, and the lower figures are simulation results. For visibility purposes, the simulation results of the quarter part were mirror-copied to the other three quadrants to show the full geometries

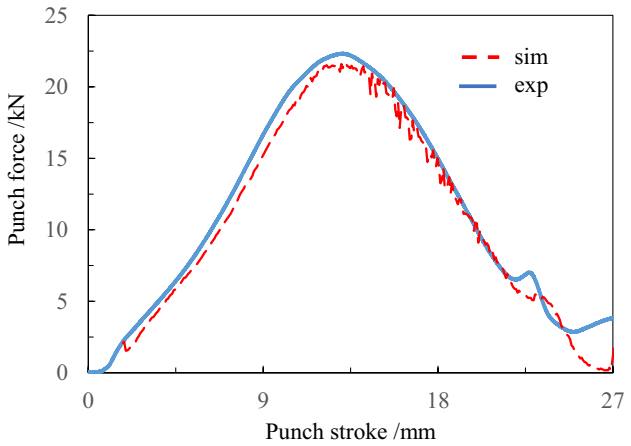

Fig. 9 Load-stroke curves obtained from the experiment and simulation

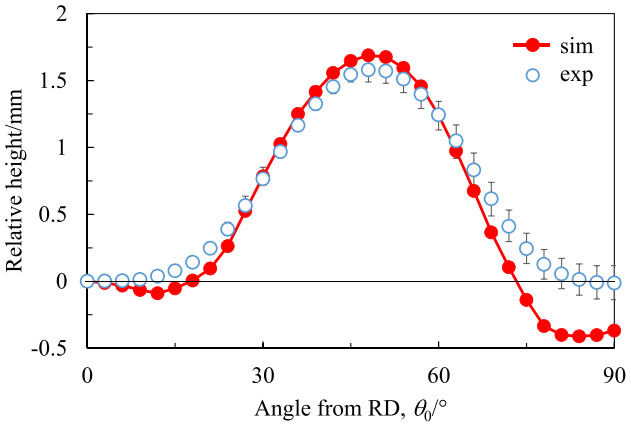

Fig. 10 Earing profiles obtained from the experiment and simulation

Figure 9 shows the experimental and simulation results of the punch force–stroke curves. In the experimental results, the punch force initially increased gradually with the stroke. The force reached a peak and began to decrease gradually at a stroke of approximately 12 mm, where the flange was detached from the upper surface of the die, as explained earlier. Then, at a stroke of approximately 21 mm, where the sheet was completely drawn into the die cavity, the force increased slightly, followed by a decrease again. Thereafter, the punch force did not converge to zero, but some forces remained. This may be because of the frictional forces between the sheet and the tools at the sidewall. The simulation results captured the qualitative tendencies observed in the experimental results, including the slight increase at a punch stroke of approximately 21 mm. However, unlike the experimental results, the force tended to converge to zero. This result indicates that the frictional forces after the sheet was completely drawn into the cavity were not reproduced well in the simulation. It should also be noted that the punch force fluctuated within the punch stroke between approximately 14 to 18 mm only in the simulation. This fluctuation occurred presumably because of numerical instabilities due to contact. As explained earlier, the sheet edge was detached from the upper surface of the die and then drawn into the die cavity during this process. The frequent and complicated changes in the contact and frictional states yielded the artificial fluctuation in the punch force. Improvements in contact and friction algorithms will be our future work.

Earing formation

Figure 10 shows the experimental and simulation earing profiles. The horizontal axis is the angle θ_0, which is the counterclockwise angle from the RD. The vertical axis is the relative cup height, where the height at the RD ($\theta_0 = 0°$) was taken as the reference and set as the origin. The relative cup height was used in this figure from the following reason. Because the gap between the die and the blank holder was set to be slightly larger than the initial thickness, tensile forces due to friction that applied to the flange was relatively small; therefore, the cup bottom became slightly rounded. This rounded bottom yielded a difficulty in accurate measurement of total cup height; thus, the relative cup height was used in Fig. 10 to remove the effect of cup bottom. On the other hand, to discuss the overall elongation in the radial direction quantitatively, lengths from the cup center will be shown later.

It was assumed that the distribution of the cup height had a four-fold symmetry. Therefore, in the experimental

results, the average of the four quadrants was evaluated for each angle.

Experimentally, the maximum height appeared at an angle of approximately 50°, and the heights at the RD and TD were similar. In the simulation results, the overall tendencies were reproduced reasonably well, but the maximum height was slightly overestimated, and the heights in the TD were seemingly underestimated.

Figure 11 shows the earing evolution along the RD, 45D, and TD as a function of the stroke. The vertical axis represents the distance from the cup center to the flange edge, as shown in Fig. 11a. In the experimental results, the length increased to a stroke of approximately 18 mm, irrespective of the direction. Thereafter, the length remained almost unchanged, that is, the earing formation was almost complete at a stroke of approximately 18 mm. The increment in length was the largest at the 45D, which was close to the position where the maximum cup height appeared. The lengths of the RD and TD were similar. The overall tendencies observed in the simulation results agreed well with the experimental results, but the lengths were slightly overestimated in the RD and 45D. Figures 10 and 11 indicate that a deviation in the cup height in the RD was apparent.

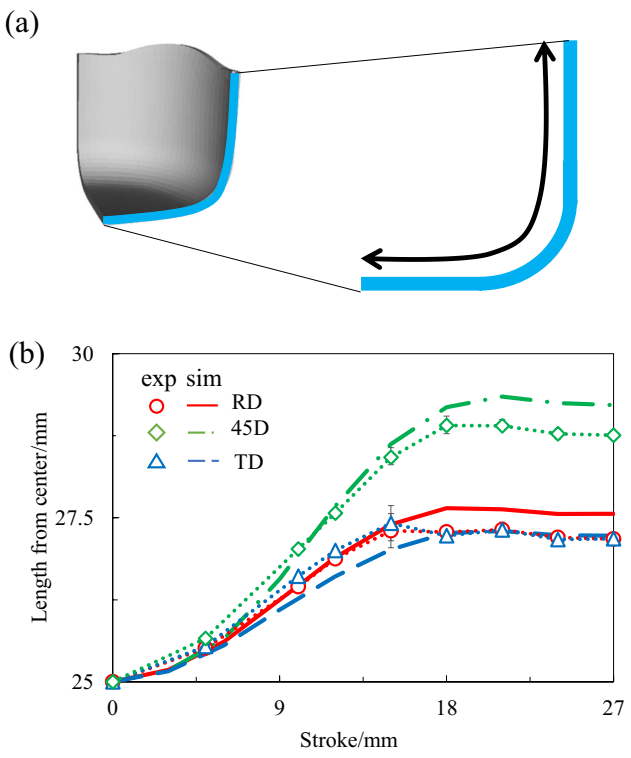

Fig. 11 Earing evolution obtained from the experiment and simulation. **a** Definition of length from the center of the cup and **b** evolution of length

Thickness evolution

Figure 12 shows the experimental and simulation results of the thickness strain distribution from the center to the edge of the cup in the RD, 45D, and TD at different punch strokes. The overall trend shown in the experimental results was as follows: the thickness strain was negligible throughout the process from 0 to 9 mm, corresponding to the punch bottom. At the punch shoulder, the thickness strain decreased from 9 to 13 mm and then increased, and it was approximately 0% again at approximately 16 mm. This distribution at the punch shoulder manifested at a punch stroke of 9 mm (Fig. 12a). The thickness strain at the punch shoulder was slightly larger in the 45D than in the RD and TD, but the overall strain distribution from 0 to 16 mm was almost independent of the direction throughout the process.

At lengths exceeding 16 mm, which corresponded to the sidewall of the cup, the thickness strain increased monotonically with the distance from the center and reached the maximum value at the edge of the cup. The magnitude of the thickness strain at the sidewall increased gradually with the punch stroke. The evolution of the thickness strain at the sidewall depended on the direction. It was initially the largest in the TD, followed by the 45D and then RD (Fig. 12a). Thereafter, the thickness strain in the RD increased as the deformation proceeded (Fig. 12b-e). Eventually, the thickness strains in the RD and the TD were almost the same and were larger than that of the 45D in the completely drawn cup (Fig. 12f). The thickness strain at the edge reached approximately 18% in the RD and the TD at strokes exceeding 21 mm, whereas it was approximately 10% in the 45D. The simulation results captured the overall experimental trends well, including the in-plane anisotropic distribution at the sidewall, while the thickening in the vicinity of the cup edge was underestimated, irrespective of the direction.

To examine the difference in the evolution of the direction dependent-thickness strain, Fig. 13 shows the evolution at the edge in the RD, 45D, and TD as a function of the punch stroke. The overall experimental trend was as follows: the thickness strain increased gradually with the stroke from the beginning to 9 mm. During this stage, the thickness in the TD was larger than that in the 45D and RD. Then, the thickness strain in the RD increased rapidly to 20 mm and became slightly larger than that in the TD. Thereafter, the change in the thickness strain was small, irrespective of the direction. Consequently, the thickness in the 45D was the smallest, while the thickness strains in the RD and TD were similar, as seen in Fig. 12.

The simulation results agreed well with the experimental results until a punch stroke of approximately 12 mm was achieved. In contrast, at larger punch strokes, thickening was underestimated, especially in the TD. Moreover, a large drop in the thickness strain occurred, especially in the RD at punch

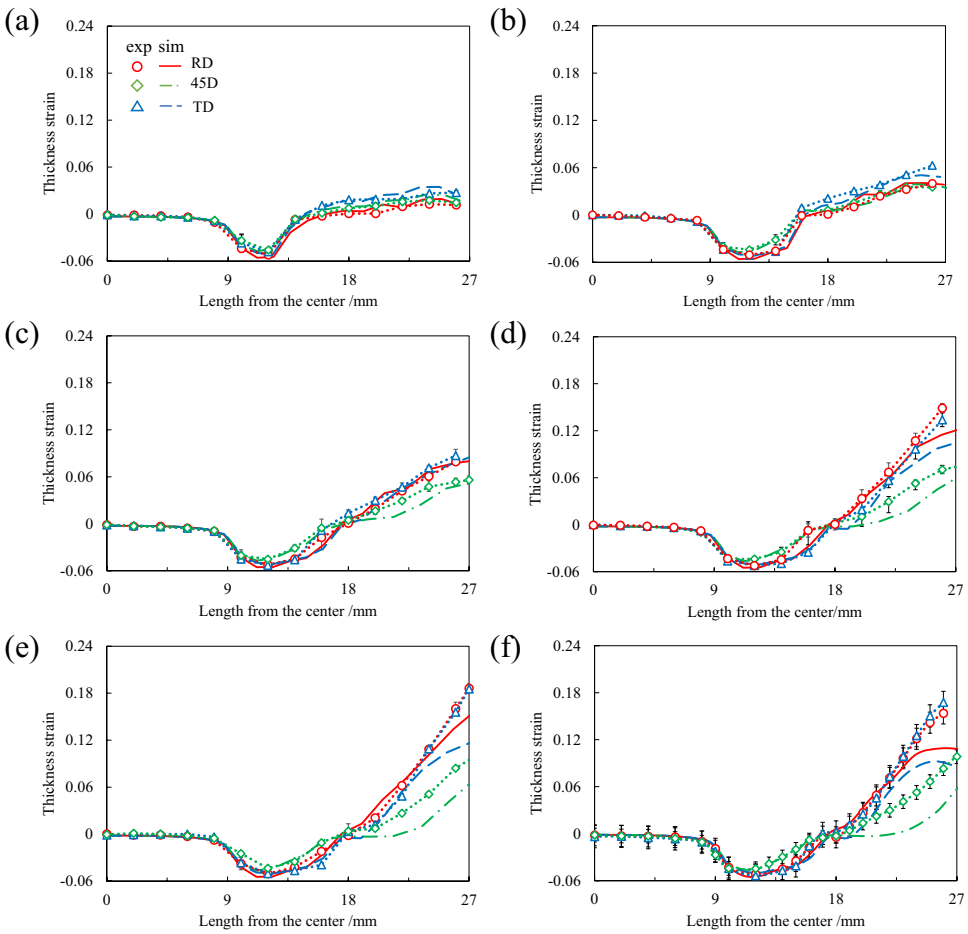

Fig. 12 Thickness strain distributions at the strokes of **a** 9, **b** 12, **c** 15, **d** 18, **e** 21, and **f** 27 mm

strokes exceeding 20 mm. This drop may be due to ironing at the sidewall. The clearance between the die and the punch was set to 1.1 mm, which was consistent with a final thickness strain in the RD of 10.6%, suggesting that the thicknesses at the cup edge in the RD and TD of the experimental results were larger than the clearance. The large thicknesses were apparent in the experiments, presumably because elastic deformation of the tools occurred when the cup edge was drawn into the cavity; thus, the effect of ironing was small and the thickness strain at a stroke exceeding 20 mm changed only slightly. Consequently, the thickness strains at the cup edge in the RD and TD were larger than the clearance. That is, large discrepancies between the experimental and simulation thickness strain appeared in the vicinity of the cup edge because the elastic deformation of the tools was not considered in the simulation. The differences in the thickness strain between the experiment and simulation should also affect the material flow, especially near the cup edge, leading to discrepancies in the cup height (Fig. 10).

The abovementioned results demonstrated that although some quantitative differences occurred, the simulation results qualitatively agreed with the experimental results, verifying the simulation models.

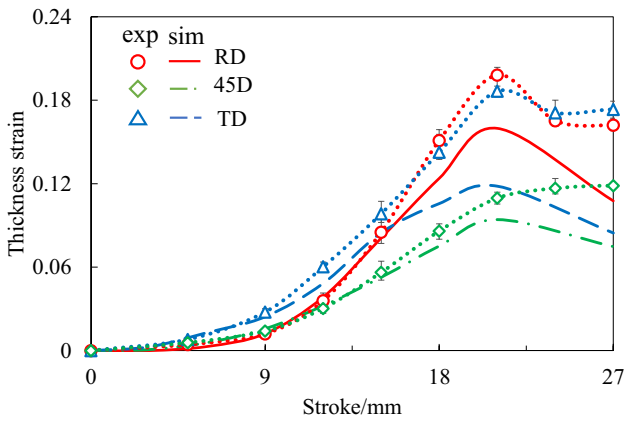

Fig. 13 Evolution of the thickness strain at the flange edge in the RD, 45D, and TD

Discussion

Mesoscopic deformation behavior

As described in the previous sections, the RD and TD deformation processes were different, although the final geometries were similar. In contrast and as already discussed in previous studies [62, 65], the mesoscopic deformation behavior of CP-Ti sheets, especially the twinning activities, largely depends on the deformation direction due to the strong rolling texture and crystal anisotropy. Hama et al. [92] studied the cyclic loading of a rolled magnesium alloy sheet with a basal texture and showed that twinning and detwinning significantly affected the *r*-value evolution, which plays an important role in earing formation in cup drawing. This observation indicates that twinning and detwinning affected the difference in the deformation processes between the RD and TD to some extent in the present drawing process. Therefore, to study the mesoscopic deformation behavior during cup drawing, the evolution of the stresses and the relative activities of the slip and twinning systems were investigated, focusing on material points along the RD and TD. The relative activity, r_i, of the family of slip or twinning systems i, is defined as:

$$r_i = \frac{\sum_{n_s}^{n} \sum_k \left|\Delta r^{(n,k)}\right|}{\sum_{n_s}^{n} \sum_j \left|\Delta r^{(n,j)}\right|} \tag{6}$$

where k is the number of the family i, j is the total number of slip and twinning systems, and n_s is the number of grains.

Figure 14 shows the stress evolution as a function of the stroke measured at points B and F in Fig. 4. It should be noted that these results were measured at integration points near the edge and the outer surface in the RD and TD. The stress components were in the x'-y'-z' co-rotational local coordinate system, where the x', y', and z' axes denote the RD, ND, and TD, respectively. The co-rotational local coordinate system was calculated using the spin tensor $\boldsymbol{W}$, that is, the antisymmetric parts of the velocity gradient tensor. Specifically, the rotation tensor $\boldsymbol{R}$, which relates the global and local coordinate systems and is initially the identity tensor, was assumed to be evolved by using the following equation [93]:

$$\dot{\boldsymbol{R}} \approx (\boldsymbol{W} - \boldsymbol{W}^{\mathrm{p}})\boldsymbol{R} \tag{7}$$

where $\boldsymbol{W}^{\mathrm{p}}$ denotes the plastic part of the spin tensor.

Figure 15 shows the evolution of the relative activities at the same points. The stresses and relative activities were calculated by averaging the results of all 400 crystal orientations at each integration point.

Based on the evolution in Figs. 14 and 15, the deformation process can be roughly divided into three stages,

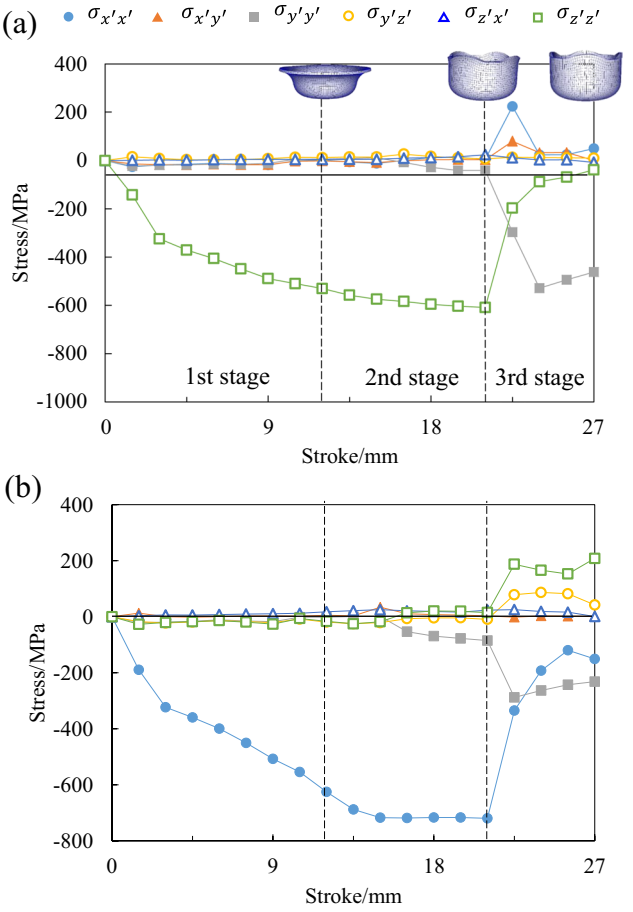

Fig. 14 Evolution of stresses at points **a** B and **b** F shown in Fig. 3

namely the first stage corresponds to the stroke range from 0 to 12 mm, the second stage from 12 to 21 mm, and the third stage from 21 to 27 mm.

In the first stage, the sheet edge was still between the blank holder and the die surface. Large compressive stresses occurred in the TD ($\sigma_{z'z'}$) at point B and the RD ($\sigma_{x'x'}$) at point F, indicating that circumferential compression of the circular sheet was dominant. The other stress components were negligible at both points B and F. During this stage, the prismatic slip systems were active at the very beginning at points B and F, followed by the activity of the pyramidal < a > slip systems. Pyramidal < a + c > -2 slip and extension twinning were also active at points B and F, respectively. The pronounced activity of extension twinning under compression in the RD was consistent with previous studies [11, 12, 62]

In the second stage, the edge was drawn into the die cavity. However, the circumferential compressive stresses were still dominant at points B and F. These stresses were very large because the equivalent plastic strains were also relatively large, and at the measured integration points, the equivalent plastic strains exceeded 50%. Pyramidal < a > slip,

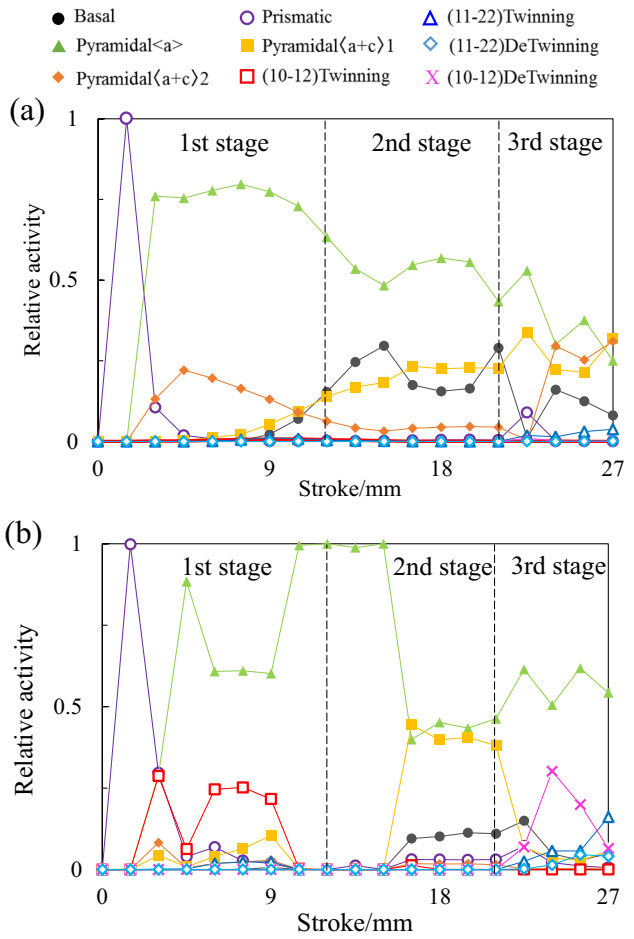

Fig. 15 Evolution of relative activities at points **a** B and **b** F shown in Fig. 3

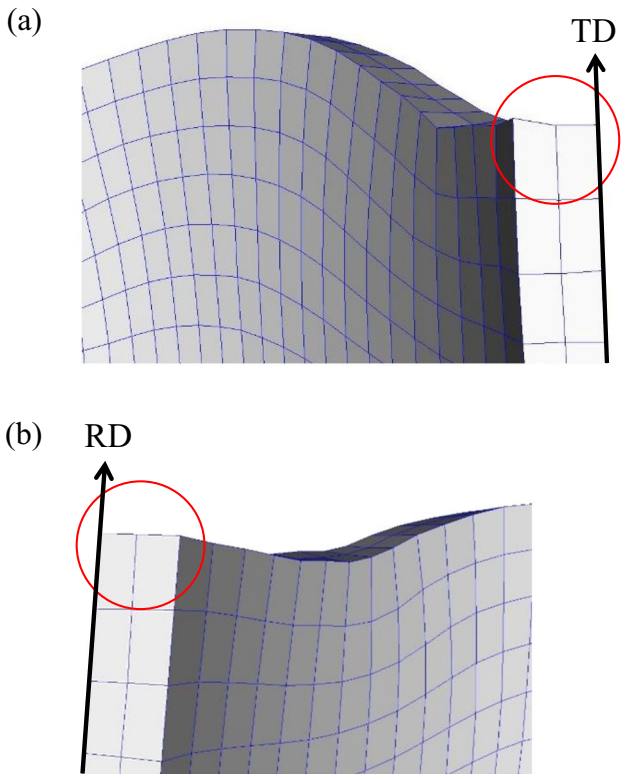

Fig. 16 Magnified figures of sheet edges of drawn cup in the (a) TD and (b) RD

basal slip, and pyramidal < a + c > -1 slip were pronounced at points B and F during this stage.

In the third stage, the outer surface of the cup near the edge tended to be stretched in the radial direction owing to the unbending at the die shoulder, and then the edge was completely drawn into the die cavity. During this stage, the stresses in the ND ($\sigma_{y'y'}$) were negative at both points. This may be because the edge was subjected to ironing deformation between the punch and the die, as discussed earlier. The negative through-thickness stress was more pronounced at point B than at point F, which is consistent with the results that the decrease in thickness was more pronounced in the RD than in the TD, as observed in Fig. 13.

Moreover, $\sigma_{y'z'}$ and $\sigma_{z'z'}$ were positive at point F. The mechanism that yielded the nonnegligible stresses at point F is presumed as follows. Because of the pronounced twinning activity under RD compression, the mesoscopic deformation in the TD was asymmetric between the inner and outer surfaces. This asymmetry yielded nonuniform through thickness deformation. Figure 16 shows the magnified figures of the sheet edges of the drawn cup. The through thickness deformation near the edge in the TD was seemingly not uniform, see Fig. 16a. It is considered that this nonuniform through thickness deformation resulted in nonnegligible stresses in the radial direction, $\sigma_{y'z'}$ and $\sigma_{z'z'}$, at point F. In contrast, the through thickness deformation was more uniform in the RD, as shown in Fig. 16b, because twinning activity was less pronounced under TD loadings. The uniform through thickness deformation in the RD resulted in much smaller stresses in the radial direction at point B than those at point F.

During this stage, pyramidal < a > slip was pronounced at points B and F. Additionally, two pyramidal < a + c > slip systems were active at point B, while extension detwinning was active at point F. Contraction twinning was also slightly active at points B and F. The compressive through-thickness stress ($\sigma_{y'y'}$) is one of the reasons for extension detwinning and contraction twinning.

These results show that the mesoscopic deformation behavior differed for the RD and TD. In particular, the twinning activities differed at points B and F, as expected from previous studies [11, 12, 62]. Although detailed results are not presented, a similar evolution of the relative activities appeared near the inner surfaces.

Texture evolution

The difference in the twinning activities at points B and F would be one of the reasons that result in a difference in texture evolution between the two points. To confirm this presumption, the microstructures were measured at points A–F shown in Fig. 4 at the punch strokes of 15 and 27 mm. Figure 17 shows the IPF maps obtained from the EBSD measurements, and Fig. 18 shows the pole figures obtained from the experiment and simulation.

The twinning activities were very small at the inner and outer surfaces in the RD (points A and B), (Fig. 17a–d), and the textures remained almost unchanged from the initial rolling texture shown in Fig. 3, regardless of the punch stroke (Fig. 18a–d). Moreover, the differences between the inner and outer surfaces were small. The predicted pole figures qualitatively agreed with the experimental results. It should be noted that the noises in the IPF maps, for example in Figs. 17b, c, and d, sometimes occur in prestrained samples with high dislocation densities [94].

Twinning was slightly active at the inner and outer surfaces in the 45D (points C and D), as shown in Fig. 17e–h. Twinning resulted in small peaks in the vicinity of the RD in the (0001) pole figures (Fig. 18e–h). It is likely that the twinning activity was more pronounced at the outer surface (point D) than at the inner surface (point C). In the simulation results, although very small peaks appeared near the RD, the change in texture was less pronounced than that of the experimental results.

At the inner and outer surfaces in the TD (points E and F), twinning was already fairly active at a punch stroke of 15 mm (Fig. 17i and k). The twinning activities yielded large

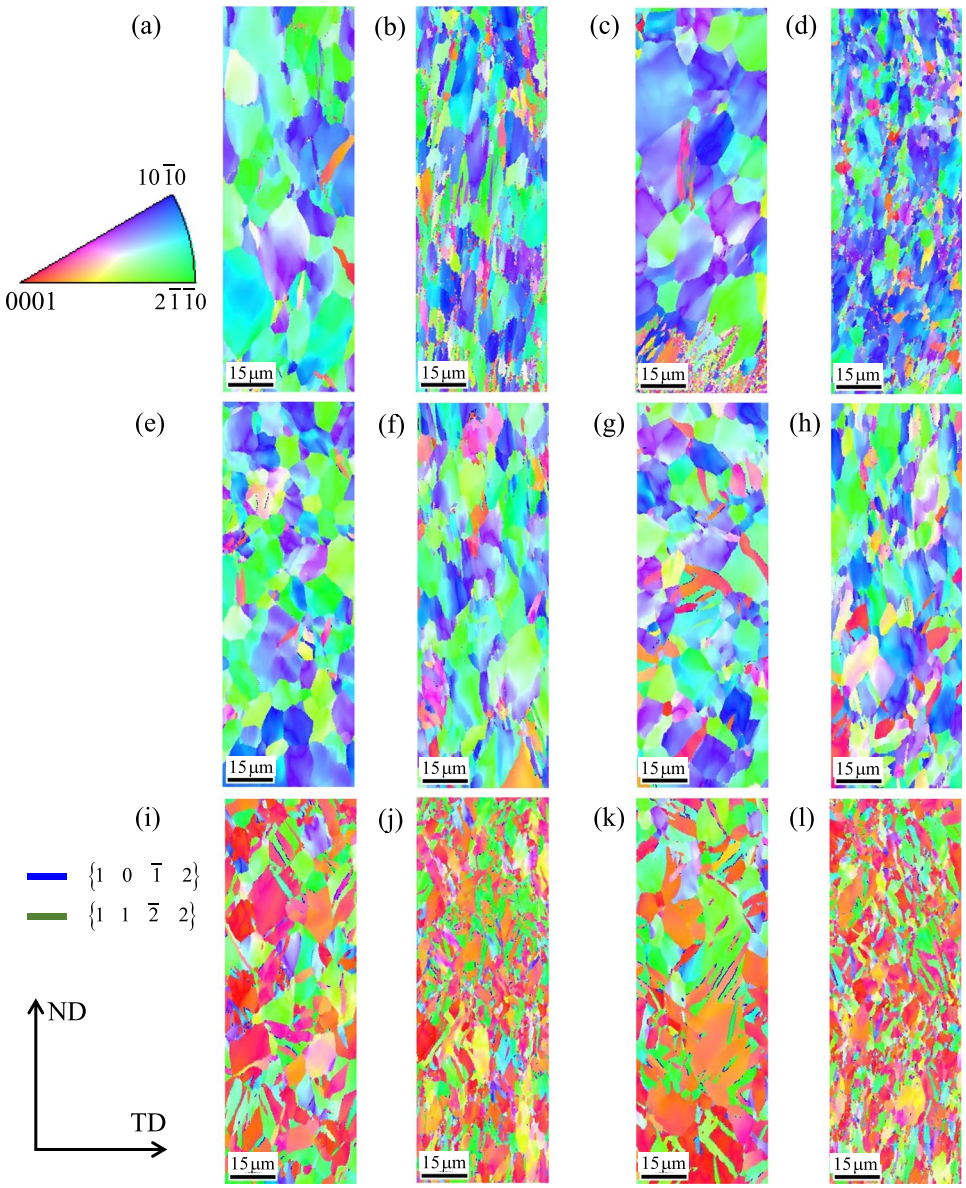

Fig. 17 IPF maps obtained from the experiment. Point A at the strokes of **a** 15 and **b** 27 mm; point B at the strokes of **c** 15 and **d** 27 mm; point C at the strokes of **e** 15 and **f** 27 mm; point D at the strokes of **g** 15 and **h** 27 mm; point E at the strokes of **i** 15 and **j** 27 mm; and point F at the strokes of **k** 15 and **l** 27 mm

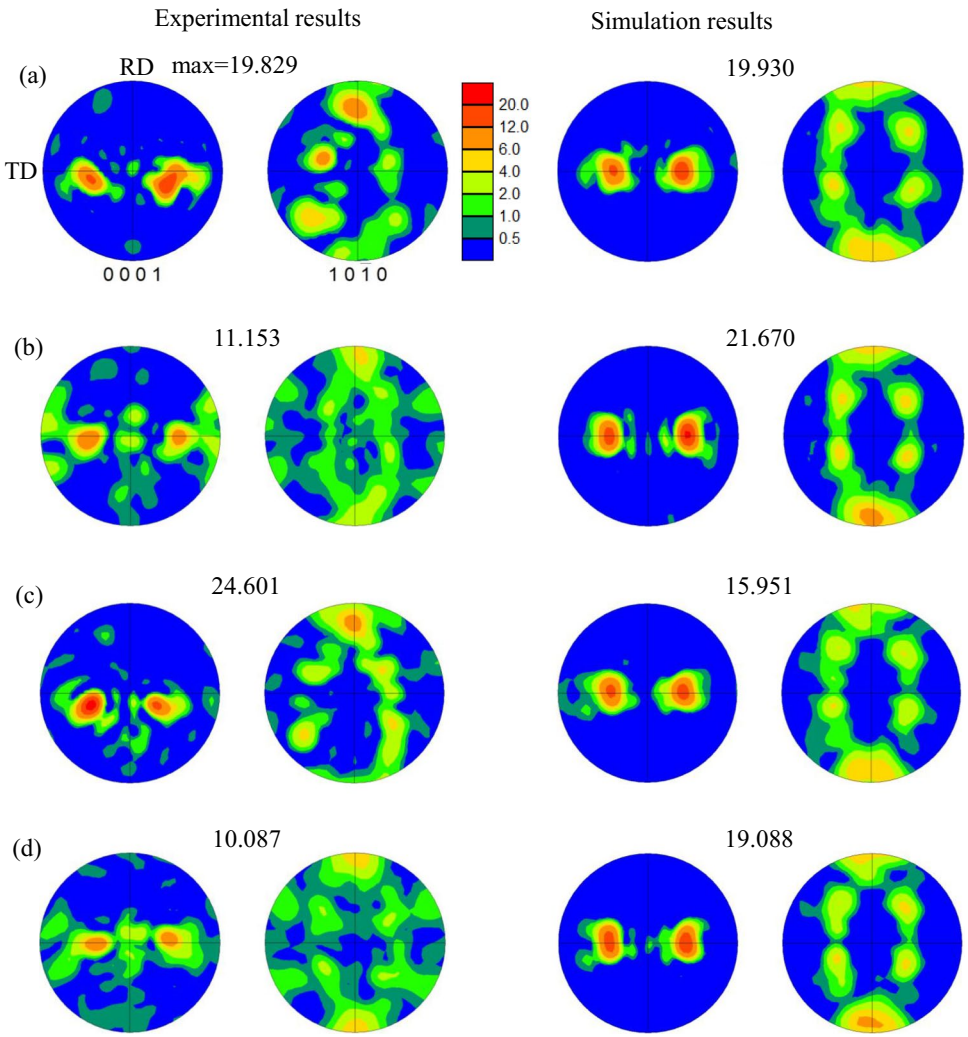

Fig. 18 Pole figures obtained from the experiments and simulations. Point A at the strokes of **a** 15 and **b** 27 mm; point B at the strokes of **c** 15 and **d** 27 mm; point C at the strokes of **e** 15 and **f** 27 mm; point D at the strokes of **g** 15 and **h** 27 mm; point E at the strokes of **i** 15 and **j** 27 mm; and point F at the strokes of **k** 15 and **l** 27 mm

peaks in the vicinity of the RD in the (0001) pole figures (Fig. 18i and k). The twinned regions further increased with the stroke (Fig. 17j and l), and the peaks in the vicinity of the RD in the (0001) pole figures became more pronounced (Fig. 18j and l). It was difficult to distinguish the difference in the extension and contraction twinning activities from the IPF maps (Fig. 17). However, these results are qualitatively consistent with the relative activities shown in Fig. 15b. The predicted pole figures also qualitatively agreed with the experimental results.

As expected, the texture evolution was notably different between the RD and TD. Because the twinning activity and the texture evolution in the 45D were similar to those in the RD, the texture evolution was more pronounced in the range from 45D to TD than from RD to 45D, although the difference in the macroscopic deformed profiles was not significant between the two ranges.

It should be noted that the grain shapes became quite anisotropic at large strains, as shown in Fig. 17, which would also affect the anisotropic deformation behavior because of anisotropy in mean free path [89]. To further increase the predictive accuracy, its effect should also be considered.

Parametric studies

Effect of twinning activity on drawability

From these discussions, it is presumed that the difference in the twinning activities in the circumferential direction affects the drawability to some extent. Specifically, twinning activities would affect the through-thickness deformation because of the basal rolling texture [92], which could also affect earing formation. To verify this assumption, a numerical experiment was conducted in which the $\{10\bar{1}2\}$ and $\{11\bar{2}2\}$ twinning systems were deactivated. The other simulation conditions remained unchanged from those in the previous simulation.

Figure 19 shows the results for the earing profile. It should be noted that the absolute height was used for the vertical axis to quantitatively compare the original and

Fig. 18 (continued)

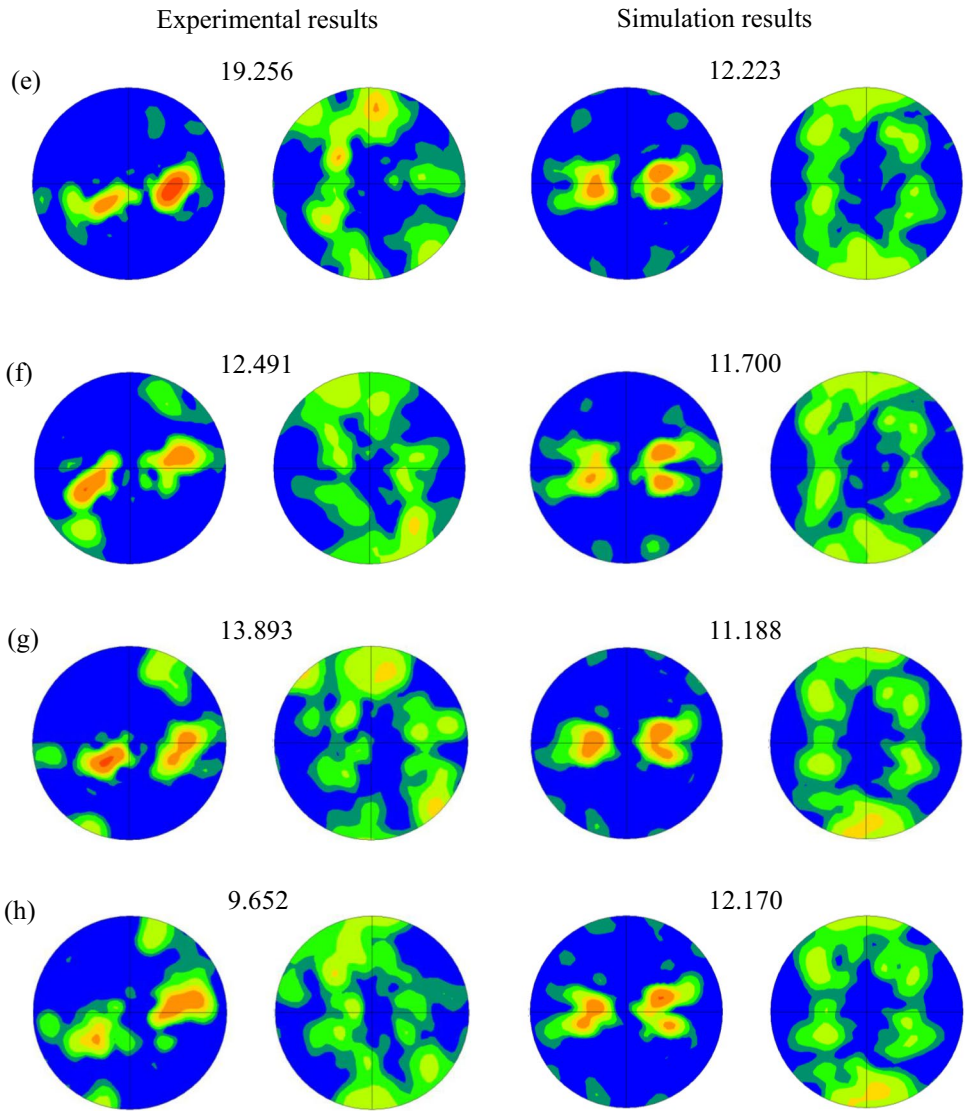

new simulation results. The heights in the vicinity of the RD remained almost unchanged from the original simulation results. In contrast, the maximum height decreased and the heights in the vicinity of the TD increased significantly; thus, the overall earing height became smaller when the twinning activities were neglected.

Figure 20 shows the thickness strain distributions along the RD, 45D, and TD at a stroke of 27 mm. In contrast to the height distribution, the thickness strain distribution along the RD changed notably when the twinning activities were neglected, while changes along the 45D and TD were small. Specifically, the thickness strains at the punch shoulder and sidewall tended to decrease along the RD. Along the TD, the thickening at the edge became larger, whereas that at the other parts remained almost unchanged. Along the 45D, the thickness strain at the punch shoulder decreased slightly, whereas that at the sidewall remained almost unchanged.

Figure 21 shows the evolution of the thickness strain at the edge in the RD, 45D, and TD. In the TD, the thickness strain decreased slightly in the first stage (0 to 12 mm stroke), which may partially result from the fact that the twinning activity at this stage was neglected. Similarly, in the third stage (21 to 27 mm stroke), the decrease in the thickness strain became smaller, which arose partially because detwinning was not active at this stage. Evidently, the change in strain evolution was consistent with the twinning activities in the TD. Moreover, the thickness strain evolution in the RD and 45D also changed. In particular, the thickness strain in the RD in the third stage decreased significantly. This result shows that twinning activities affect the drawability not only along the TD, where pronounced twinning activities were observed, but also over the entire region. Therefore, it is important to consider the twinning activities to accurately predict the forming processes of CP-Ti sheets.

Fig. 18 (continued)

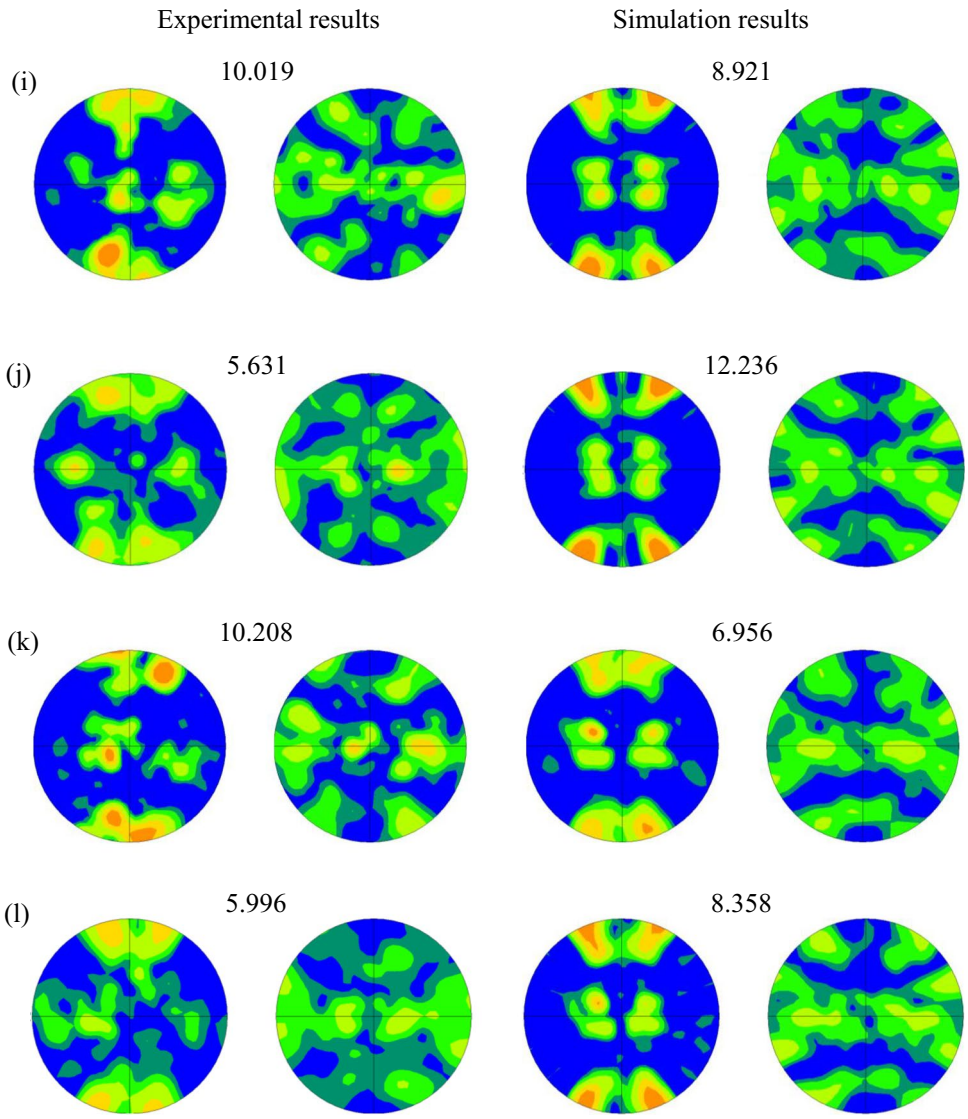

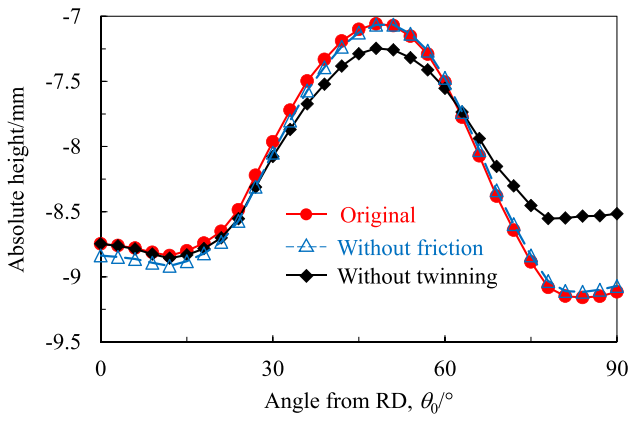

Fig. 19 Simulation results of the earing profile without twinning and without friction

Effect of friction

Ironing occurred at the sidewall during the drawing process; therefore, the deformations at the sidewall, including the thickness and cup height, are dependent on the friction between the sheet and the tools. Similarly, twinning activities will change when the frictional conditions are changed. However, it is difficult to examine this experimentally because galling easily occurs during drawing processes of CP-Ti [77]. Therefore, a drawing simulation was conducted without considering friction to numerically examine the effect of friction.

Figure 19 shows the earing profile in terms of absolute height. When friction was neglected, the height in the vicinity of the RD slightly decreased, whereas that of the TD slightly increased; thus, the difference in the height between the RD and TD decreased. This result indicates that a large difference in the height between the RD and

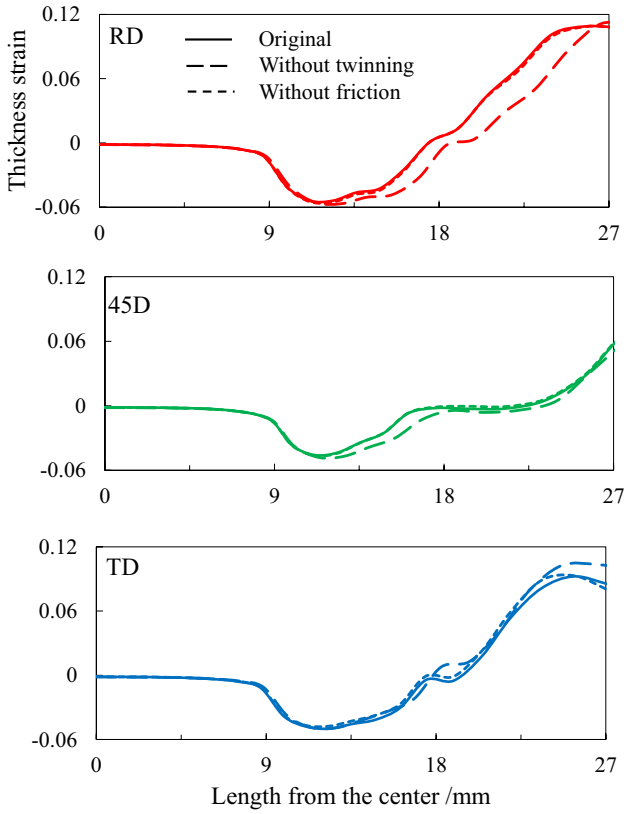

Fig. 20 Thickness strain distributions at a 27 mm-stroke in the RD, 45D, and TD

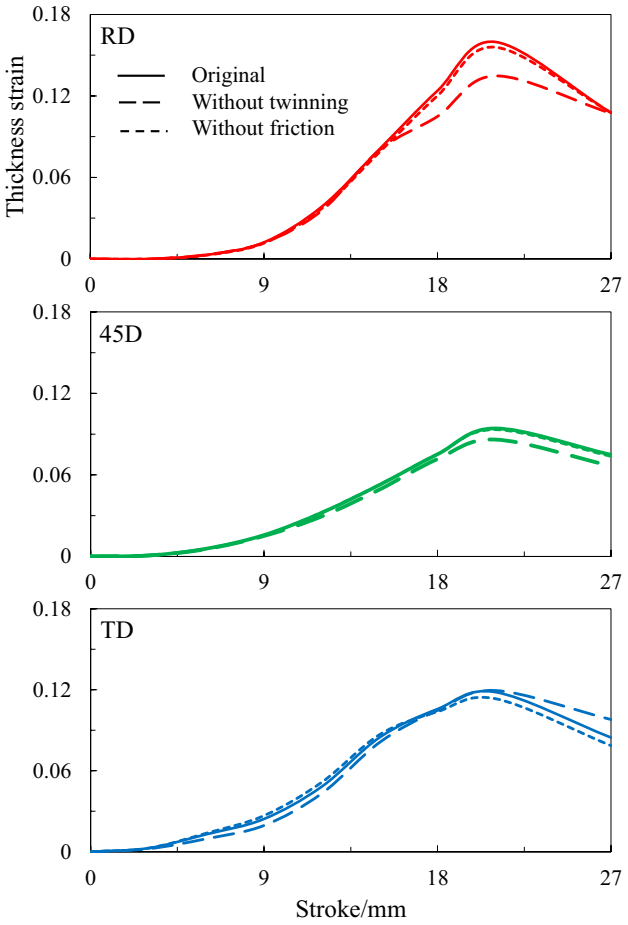

Fig. 21 Evolution of the thickness strain at the flange edge in the RD, 45D, and TD

TD appeared in the original simulation result partially because of friction.

Figure 22 shows the evolution of the relative activities. Because evidently different evolutions were observed between the inner and outer surfaces, unlike the original results, the results near both surfaces are reported. When friction was not considered, extension twinning slightly increased in the TD (points E and F) in the first stage, whereas in the third stage, extension detwinning was negligible only near the inner surface (point E). In contrast, the slip and twinning activities were hardly affected by the friction in the RD (points A and B). These results show that the frictional condition affected the twinning activities to some extent, particularly in the TD.

Figure 20 shows the thickness strain distributions along the RD, 45D, and TD on the drawn cup. The distributions along the RD and 45D were hardly affected by friction.

In contrast, the thickness slightly increased at the sidewall along the TD, whereas it was smaller at the edge. Figure 21 shows the evolution of the thickness strain at the edges. In the TD, the thickness was slightly larger during the first and second stages, whereas it was smaller during the third stage. The strain in the RD at a stroke of 21 mm also decreased, but the strain at a stroke of 27 mm remained almost unchanged because the final thickness in the RD was determined by the clearance between the punch and the tools due to ironing.

These results demonstrate that the deformation along the TD was more easily affected by the friction than in other regions, partially because of the change in twinning activity. It should be noted that the smaller thickness in the TD in the third stage contradicted the tendency that is expected from the reduced detwinning activity because material flow in the radial direction was facilitated due to ironing when friction was neglected. The above discussion indicates that the change in the cup height distribution was more affected by the change in material flow due to ironing than by the change in twinning activities.

Conclusion

In this study, experiments and crystal plasticity finite-element simulations of a cup drawing process of a cold-rolled Grade 2 CP-Ti sheet were conducted, and the applicability of the crystal plasticity model to the forming process was

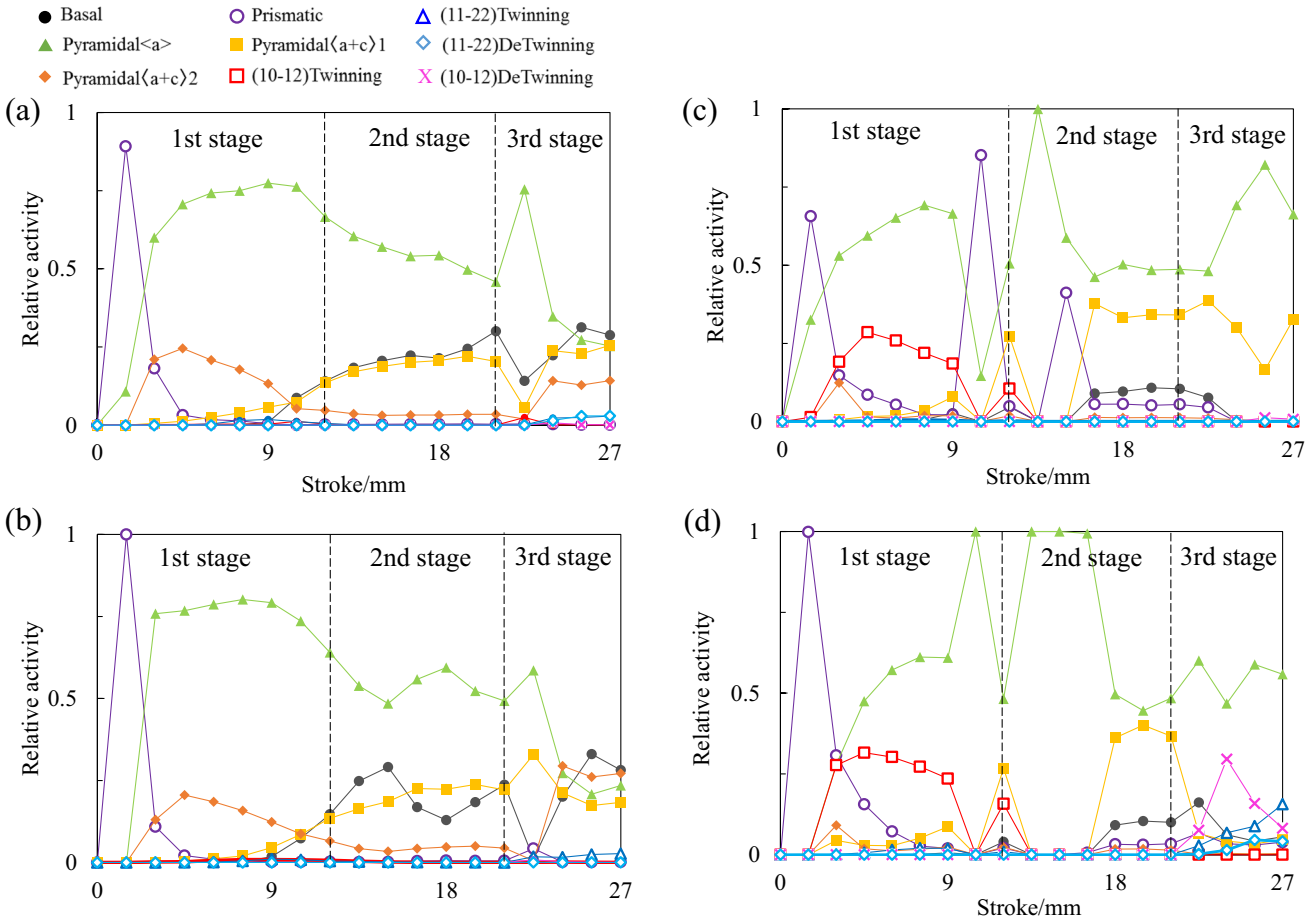

Fig. 22 Evolution of the relative activities obtained without considering friction at points **a** A, **b** B, **c** E, and **d** F shown in Fig. 3

examined. The drawability, including earing formation, evolution of the thickness distribution, and texture evolution, was examined in detail. Moreover, parametric studies were conducted to discuss the effects of the simulation conditions, including twinning activity and friction, on the drawability. The main conclusions of this study are summarized as:

(1) In the experiments, the maximum cup height appeared at an angle from the RD of approximately 50 °, and the heights at the RD and TD were similar. The evolution of the thickness strain distribution at the sidewall depended strongly on the direction. That is, the thickness strain was initially the largest in the TD, but thereafter that in the RD increased, and eventually, the thickness strains in the RD and the TD were similar and were larger than that of the 45D. The simulation results qualitatively captured these tendencies in the macroscopic deformation processes, but from a quantitative perspective, non-negligible discrepancies emerged, including the cup height in the TD and the thickening at the cup edge in the RD and TD.

(2) Twinning activity during drawing was the largest in the TD, followed by the 45D and then the RD. The twinning activity and texture evolution in the 45D were similar to those in the RD; thus, the texture evolution was more pronounced in the range from 45D to TD than from RD to 45D. The overall trends in the simulation agreed well with those of the experiment, although the texture evolution in the 45D was less pronounced.

(3) The simulation not considering twinning showed that the twinning activities affected the deformation behavior, including cup height and thickness strain distribution, not only along the TD where pronounced twinning activities were observed, but also over the entire region. These results suggest that it is important to consider twinning activities for an accurate prediction of the forming processes of CP-Ti sheets.

(4) When friction was neglected in the simulation, the difference in the cup height between the RD and the TD slightly decreased, and the thickness strain distribution in the TD changed slightly, that is, it became larger at the sidewall and smaller at the edge. These results

indicate that the deformation along the TD was more easily affected by friction than at the other regions. The changes in the deformation behavior might result from both the change in material flow due to ironing and the change in twinning activities.

Appendix 1

Effect of numbers of initial orientations and finite elements on cup drawing simulation

Two additional cup drawing simulations were conducted. The number of orientations assigned to each integration point was set to 100 in the first case, while a finite element model with 1000 elements were used in the second case. Other simulation conditions remained unchanged. The pole figures obtained with the 100 orientations used in the first case are shown in Fig. 23a. The distributions are slightly different from those of the experimental results (Fig. 3a) especially in the $(10\bar{1}0)$ pole figure and, moreover, the maximum intensity was slightly larger. Figure 23b shows the finite element model with 1000 elements used in the second case. The numbers of elements in the radial and circumferential directions were smaller than those of the original model (Fig. 5), while the number of elements through the thickness remained unchanged.

Figure 23c and d show the earing profiles and evolution of the thickness strain at the flange edge. The earing profiles were almost independent of the simulation condition. In contrast, the evolution of the thickness strains depended on the simulation condition. Especially, the evolution in the RD and TD differed largely. These results show that it is important to use appropriate simulation conditions to discuss strain evolution although the results of earing profile were not affected by the conditions.

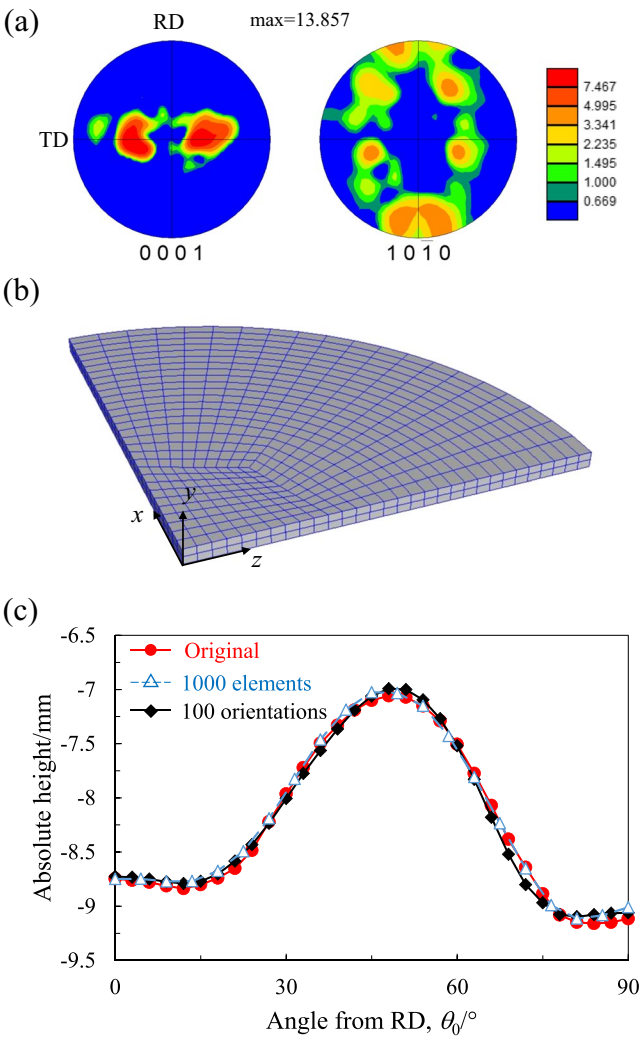

Fig. 23 Simulation results obtained using different numbers of orientations or finite elements. **a** The initial pole figures for 100 orientations, **b** the finite-element model with 1000 elements, **c** earing profiles, and **d** evolution of the thickness strain at the flange edge

Fig. 23 (continued)

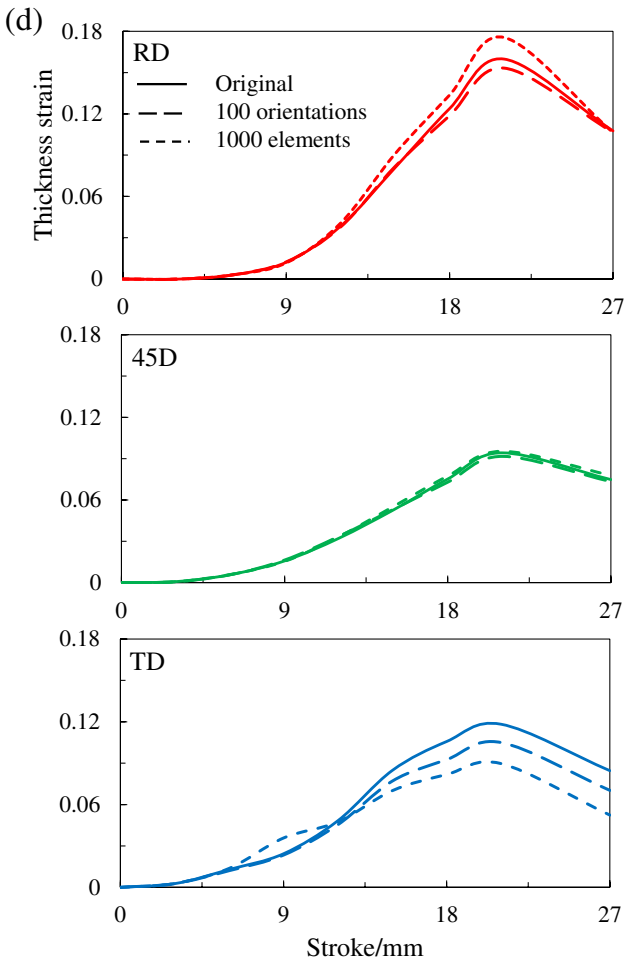

Appendix 2

Determination of material parameters

Based on a previous study for a Grade 1 CP-Ti sheet [62], it was first presumed that the CRSS was the smallest for prismatic slip, followed in order by pyramidal < a > slip and pyramidal < a + c > slip. As in a previous study, the rank of the CRSS for basal slip was adjusted to reproduce experimental results. The CRSS for pyramidal < a + c > slip was initially assumed to be larger than twice as large as that for prismatic slip. Because twinning activities are smaller in a Grade 2 CP-Ti sheet than those in a Grade 1 CP-Ti sheet [11, 12], the rank of the CRSSs for twinning used in a previous study could not be utilized in this study. Our preliminary study for a Grade 2 CP-Ti sheet [95] reported that the CRSSs for twinning were set to be comparable or larger than those of pyramidal < a + c > slip to fit evolution of twin volume fraction. Therefore, the same assumption was used for initial guess also in this study.

Then, the hardening parameters were calibrated. Considering the role of each slip and twinning system on the work-hardening behavior, the parameters for prismatic slip and contraction twinning were primarily calibrated by referring to the stress–strain curve and the evolution of the *r*-value under RD tension. Similarly, the parameters for pyramidal < a > and basal slip were calibrated using the results of TD tension, whereas those of extension twinning were calibrated using the results of RD compression. These steps were repeated several times to obtain good fits with the experimental results under RD, 45D, and TD loadings with a single set of parameters. The reader is referred to a previous study [62] for the basic calibration procedures.

Acknowledgements The authors would like to acknowledge Mr. Sohei Uchida of the Osaka Research Institute of Industrial Science and Technology for assisting with the EBSD. This study was supported by the Japan Society for the Promotion of Science (JSPS) Grants-in-Aid for Scientific Research (KAKENHI) Grant number 20H02480 and the Amada Foundation Grant number AF-2019004-A3. We would like to thank Editage (www.editage.com) for English language editing.

References

1. Fujii H, Takahashi K, Yamashita Y (2003) Application of titanium and its alloys for automobile parts. Nippon Steel Technical Report 88:70–75
2. Sing SL, Wiria FE, Yeong WY (2018) Selective laser melting of lattice structures: a statistical approach to manufacturability and mechanical behavior. Robotics and Computer-Integrated Manufacturing 49:170–180
3. Lee D, Backofen WA (1966) An experimental determination of the yield locus for titanium and titanium-alloy sheet. Trans Am Inst Min Metall Pet Eng 236:1077–1084
4. Mullins S, Patchett BM (1981) Deformation microstructures in titanium sheet metal. Metall Trans A 12:853–863
5. Ishiyama S (2006) Plastic deformation and press formability of C.P. titanium sheet. Titan Japan 54:42–51 **(in Japanese)**
6. Huang X, Suzuki K, Chino Y (2010) Improvement of stretch formability of pure titanium sheet by differential speed rolling. Scripta Mater 63:473–476
7. Nixon ME, Cazacu O, Lebensohn RA (2010) Anisotropic response of high-purity α-titanium: experimental characterization and constitutive modeling. Int J Plast 26:516–532
8. Ishiki M, Kuwabara T, Hayashida Y (2011) Measurement and analysis of differential work hardening behavior of pure titanium sheet using spline function. IntJ Mater Form 4:193–204
9. Bouvier S, Benmhenni N, Tirry W, Gregory F, Nixon ME, Cazacu O, Rabet L (2012) Hardening in relation with microstructure evolution of high purity α-titanium deformed under monotonic and cyclic simple shear loadings at room temperature. Mater Sci Eng, A 535:12–21
10. Roth A, Lebyodkin MA, Lebedkina TA, Lecomte J-S, Richeton T, Amouzou KEK (2014) Mechanisms of anisotropy of mechanical properties of α-titanium in tension conditions. Mater Sci Eng, A 596:236–243
11. Hama T, Nagao H, Kobuki A, Fujimoto H, Takuda H (2015) Work-hardening and twinning behaviors in a commercially pure titanium sheet under various loading paths. Mater Sci Eng, A 620:390–398
12. Yi N, Hama T, Kobuki A, Fujimoto H, Takuda H (2016) Anisotropic deformation behavior under various strain paths in commercially pure titanium grade 1 and grade 2 sheets. Mater Sci Eng, A 655:70–85
13. Won JW, Choi SW, Yeom JT, Hyu YT, Lee CS, Park SH (2017) Anisotropic twinning and slip behaviors and their relative activities in rolled alpha-phase titanium. Mater Sci Eng, A 698:54–62
14. Baral M, Hama T, Knudsen E, Korkolis YP (2018) Plastic deformation of commercially-pure titanium: experiments and modeling. Int J Plast 105:164–194
15. Rossi FD, Dube CA, Alexander BH (1953) Mechanism of plastic flow in titanium –determination of slip and twinning elements. J Metals 5:257–265
16. Anderson EA, Jilson DC, Dunbar SR (1953) Deformation mechanisms in alpha titanium. J Metals 5:1191–1197
17. Conrad H (1981) Effect of interstitial solutes on the strength ductility of titanium. Prog Mater Sci 26:123–403
18. Murayama Y, Obara K, Ikeda K (1987) Effect of twinning on the deformation behavior of textured sheets of pure titanium in uniaxial tensile test. Transactions of the Japan Institute of Metals 28:564–578
19. Chichili DR, Ramesh KT, Hemker KJ (1998) The high-strain-rate response of alpha-titanium: experiments, deformation mechanisms and modeling. Acta Mater 46:1025–1043
20. Nemat-Nasser S, Guo WG, Cheng JY (1999) Mechanical properties and deformation mechanism of a commercially pure titanium. Acta Mater 47:3705–3720
21. Wang L, Barabash RI, Yang Y, Bieler TR, Crimp MA, Eisenlohr P, Liu W, Ice GE (2011) Experimental characterization and crystal plasticity modeling of heterogeneous deformation in polycrystalline α-Ti. Metall and Mater Trans A 42:626–635
22. Warwick JLW, Jones NG, Rahman KM, Dye D (2012) Lattice strain evolution during tensile and compressive loading of CP Ti. Acta Mater 60:6720–6731
23. Wang L, Zheng Z, Phukan H, Kenesei P, Park J-S, Lind J, Suter RM, Bieler TR (2017) Direct measurement of critical resolved shear stress of prismatic and basal slip in polycrystalline Ti using high energy X-ray diffraction microscopy. Acta Mater 132:598–610
24. Paton NE, Backofen WA (1970) Plastic deformation of titanium at elevated temperatures. Metallurgical Transactions 1:2839–2847
25. Numakura H, Minonishi Y, Koiwa M (1986) <1123>{1011} slip in titanium polycrystals at room temperature. Scr Metall 20:1581–1586
26. Christian JW, Mahajan S (1995) Deformation twinning. Prog Mater Sci 39:1–157
27. Chun YB, Yu SH, Semiatin SL, Hwang SK (2005) Effect of deformation twinning on microstructure and texture evolution during cold rolling of CP-titanium. Mater Sci Eng, A 398:209–219
28. Battaini M, Pereloma EV, Davies CHJ (2007) Orientation effect on mechanical properties of commercially pure titanium at room temperature. Metall and Mater Trans A 38:276–285
29. Tirry W, Nixon M, Cazacu O, Coghe F, Rabet L (2011) The importance of secondary and ternary twinning in compressed Ti. Scripta Mater 64:840–843
30. Tirry W, Bouvier S, Benmhenni N, Hammami W, Habraken AM, Coghe F, Schryvers D, Rabet L (2012) Twinning in pure Ti subjected to monotonic simple shear deformation. Mater Charact 72:24–36
31. Kuwabara T, Katami C, Kikuchi M, Shindo T, Ohwue T (2001) Cup drawing of pure titanium sheet -finite element analysis and experimental validation-. Proceedings of 7th International Conference NUMIFORM 2001 781–787.
32. Liu J, Chen I, Chou T, Chou S (2002) On the deformation texture of square-shaped deep-drawing commercially pure Ti sheet. Mater Chem Phys 77:765–772
33. Usuda M (2002) Press formability of commercially pure titanium sheets. Nippon Steel Technical Report 85:24–30
34. Marciniak Z, Duncan JL, Hu SJ (2002) Mechanics of sheet metal forming. Butterworth Heinemann, Oxford 117–128.
35. Raemy C, Manopulo N, Hora P (2017) On the modelling of plastic anisotropy, asymmetry and directional hardening of commercially pure titanium: a planar Fourier series based approach. Int J Plast 91:182–204
36. Gokyu I, Okubo T, Tanabe T, Kitanaka K (1972) The deep drawability of titanium sheet. Journal of Japan Institute of Metals and Materials 36:972–977 **(in Japanese)**
37. Kawai N, Hayashi N, Takayama K (1987) Assessment of deep-drawability of commercially pure titanium sheets based on the texture change during processing. Transactions of the Japan Society of Mechanical Engineers 53:763–770 **(in Japanese)**
38. Akamatsu T, Ukita S, Miyasaka K, Shi M (1995) Deep drawing of commercially pure titanium sheets. ISIJ Int 35:56–62
39. Liu S, Chou S (1999) Study on the microstructure and formability of commercially pure titanium in two-temperature deep drawing. J Mater Process Technol 95:65–70
40. Satoh J, Gotoh M, Maeda Y (2003) Stretch-drawing of titanium sheets. J Mater Process Technol 139:201–207
41. Chen F-K, Chiu K-H (2005) Stamping formability of pure titanium sheets. J Mater Process Technol 170:181–186
42. Le Port A, Toussaint F, Arrieux R (2009) Finite element study and sensitive analysis of the deep-drawing formability of commercially pure titanium. IntJ Mater Form 2:121–129

43. Zhang X-H, Tang B, Zhang X-L, Kou H-C, Li J-S, Zhou L (2012) Microstructure and texture of commercially pure titanium in cold deep drawing. Transactions of Nonferrous Metals Society of China 22:496–502
44. Ohwue T, Sato K, Kobayashi Y (2013) Analysis of earring in circular-shell deep-drawing test. Transactions of the Japan Society of Mechanical Engineers 79:595–608
45. Singh A, Basak S, Prakash PS, Lin Roy GG, Jha MN, Mascarenhas M, Panda SK (2018) Prediction of earing defect and deep drawing behavior of commercially pure titanium sheets using CPB06 anisotropy yield theory. J Manuf Process 33:256–267
46. Hill R (1948) A theory of the yielding and plastic flow of anisotropic metals. Proceedings of the Royal Society A 193:281–297
47. Hill R (1990) Constitutive modelling of orthotropic plasticity in sheet metals. J Mech Phys Solids 38:405–417
48. Barlat F, Lian J (1989) Plastic behavior and stretchability of sheet metals. Part I A yield function for orthotropic sheets under plane stress conditions. Int J Plast 5:51–66
49. von Mises R (1913) Mechanik der festen korper im plastisch deformablen zustand. Nachrichten von der Gesellschaft der Wissenschaften zu Göttingen 1:582–592
50. Cazacu O, Plunkett B, Barlat F (2006) Orthotropic yield criterion for hexagonal closed packed metals. Int J Plast 22:1171–1194
51. Plunkett B, Cazacu O, Barlat F (2008) Orthotropic yield criteria for description of the anisotropy in tension and compression of sheet metals. Int J Plast 24:847–866
52. Wu X, Kalidindi SR, Necker C, Salem AA (2007) Prediction of crystallographic texture evolution and anisotropic stress–strain curves during large plastic strains in high purity α-titanium using a Taylor-type crystal plasticity model. Acta Mater 55:423–432
53. Yang Y, Wang L, Bieler TR, Eisenlohr P, Crimp MA (2011) Quantitative atomic force microscopy characterization and crystal plasticity finite element modeling of heterogeneous deformation in commercial purity titanium. Metall and Mater Trans A 42:636–644
54. Gurao NP, Kapoor R, Suwas S (2011) Deformation behaviour of commercially pure titanium at extreme strain rates. Acta Mater 59:3431–3446
55. Zambaldi C, Yang Y, Bieler TR (2012) Orientation informed nanoindentation of α-titanium: indentation pileup in hexagonal metals deforming by prismatic slip. J Mater Res 27:356–367
56. Benmhenni N, Bouvier S, Brenner R, Chauveau T, Bacroix B (2013) Micromechanical modelling of monotonic loading of CP α-Ti: correlation between macroscopic and microscopic behavior. Mater Sci Eng, A 573:222–233
57. Kowalczyk-Gajewska K, Sztwiertnia K, Kawalko J, Wierzbanowski K, Wronski M, Frydrich K, Stupkiewicz S, Petryk H (2015) Texture evolution in titanium on complex deformation paths: experiment and modelling. Mater Sci Eng, A 637:251–263
58. Sinha S, Ghosh A, Grao NP (2016) Effect of initial orientation on the tensile properties of commercially pure titanium. Phil Mag 96:1485–1508
59. Amouzou KEK, Richeton T, Roth A, Lebyodkin MA, Lebedkina TA (2016) Micromechanical modeling of hardening mechanisms in commercially pure alpha-titanium in tensile condition. Int J Plast 80:222–240
60. Gloaguen D, Girault B, Fajoui J, Klosek V, Moya M-J (2016) In situ lattice strains analysis in titanium during a uniaxial tensile test. Mater Sci Eng, A 662:395–403
61. Marchenko A, Mazière M, Forest S, Strudel J-L (2016) Crystal plasticity simulation of strain aging phenomena in α-titanium at room temperature. Int J Plast 85:1–33
62. Hama T, Kobuki A, Takuda H (2017) Crystal-plasticity finite-element analysis of anisotropic deformation behavior in commercially pure titanium grade 1 sheet. Int J Plast 91:77–108
63. Wronski M, Arul Kumar M, Capolungo L, McCabe RJ, Wierzbanowski A, Tomé CN (2018) Deformation behavior of CP-titanium: experiment and crystal plasticity modeling. Mater Sci Eng, A 724:289–297
64. Frydrych K, Kowalczyk-Gajewska K (2018) Microstructure evolution in cold-rolled pure titanium: modeling by the three-scale crystal plasticity approach accounting for twinning. Metall and Mater Trans A 49A:3610–3623
65. Ma C, Wang H, Hama T, Guo X, Mao X, Wang J, Wu P (2019) Twinning and detwinning behaviors of commercially pure titanium sheets. Int J Plast 121:261–279
66. Baudoin P, Hama T, Takuda H (2019) Influence of critical resolved shear stress ratios on the response of a commercially pure titanium oligocrystal: crystal plasticity simulations and experiment. Int J Plast 115:111–131
67. Wang J, Zecevic M, Knezevic M, Beyerlein IJ (2020) Polycrystal plasticity modeling for load reversals in commercially pure Titanium. Int J Plast 125:294–313
68. Xiong Y, Karamched P, Nguyen C, Collins DM, Magazzeni CM, Tarleton E, Wilkinson AJ (2020) Cold creep of titanium: analysis of stress relaxation using synchrotron diffraction and crystal plasticity simulations. Acta Mater 199:561–577
69. Nakamachi E, Xie CL, Harimoto M (2001) Drawability assessment of bcc steel sheet by using elastic/crystalline viscoplastic finite element analyses. Int J Mech Sci 43:631–652
70. Nakamachi E, Xie CL, Morimoto H, Morita K, Yokoyama N (2002) Formability assessment of fcc aluminum alloy sheet by using elastic/crystalline viscoplastic finite element analysis. Int J Plast 18:617–632
71. Raabe D, Wang Y, Roters F (2005) Crystal plasticity simulation study on the influence of texture on earing in steel. Comput Mater Sci 34:221–234
72. Tang W, Zhang S, Peng Z, Li D (2009) Simulation of magnesium alloy AZ31 sheet during cylindrical cup drawing with rate independent crystal plasticity finite element method. Comput Mater Sci 46:393–399
73. Shi Y, Jin H, Wu PD (2018) Analysis of cup earing for AA3104-H19 aluminum alloy sheet. European Journal of Mechanics / A Solids 69:1–11
74. Barrett TJ, Knezevic M (2019) Deep drawing simulations using the finite element method embedding a multi-level crystal plasticity constitutive law: experimental verification and sensitivity analysis. Computational Methods in Applied Mechanics and Engineering 354:245–270
75. Barrett TJ, McCabe RJ, Brown DW, Clausen B, Vogel SC, Knezevic M (2020) Predicting deformation behavior of α-uranium during tension, compression, load reversal, rolling, and sheet forming using elaso-plastic, multi-level crystal plasticity coupled with finite elements. Journal of the Mechanics and Physics of Solids 138:103924.
76. Feng Z, Yoon S-Y, Choi J-H, Barrett TJ, Zecevic M, Barlat F, Knezevic M (2020) A comparative study between elasto-plastic self-consistent crystal plasticity and anisotropic yield function with distortional hardening formulations for sheet metal forming. Mechanics and Materials 148:103422.
77. Aizawa T, Itoh K-i, Fukuda T (2020) SiC-coated SiC die for galling-free forging of pure titanium. Mater Trans 61:282–288
78. Hama T, Takuda H (2011) Crystal-plasticity finite-element analysis of inelastic behavior during unloading in a magnesium alloy sheet. Int J Plast 27:1072–1092
79. Kawka M, Makinouchi A (1995) Shell-element formulation in the static explicit FEM code for the simulation of sheet stamping. J Mater Process Technol 50:105–115
80. Hama T, Nagata T, Teodosiu C, Makinouchi A, Takuda T (2008) Finite-element simulation of springback in sheet metal

forming using local interpolation for tool surfaces. Int J Mech Sci 50:175–192
81. Yamamura N Kuwabara T Makinouchi A (2002) Springback simulations for stretch-bending and draw-bending processes using the static explicit FEM code, with an algorithm for canceling non-equilibrated forces. In: Proceedings of the fifth NUMISHEET, Jeju, Korea : 25–30.
82. Yamada Y, Yoshimura N, Sakurai T (1968) Plastic stress-strain matrix and its application for the solution of elastic–plastic problems by the finite element method. Int J Mech Sci 10:343–354
83. Hughes TJR (1980) Generalization o selective integration procedures to anisotropic and nonlinear media. Int J Numer Meth Eng 15–9:1413–1418
84. Zecevic M, Beyerlein IJ, Knezevic M (2017) Coupling elasto-plastic self-consistent crystal plasticity and implicit finite elements: applications to compression, cyclic tension-compression, and bending to large strains. Int J Plast 93:187–211
85. Zecevic M Knezevic M (2019) An implicit formulation of the elasto-plastic self-consistent polycrystal plasticity model and its implementation in implicit finite elements. Mechanics of Materials 136: 103065.
86. Taylor GI (1938) Plastic strain in metals. Journal of Institute of Metals 62:307–324
87. Asaro RJ, Needleman A (1985) Texture development and strain hardening in rate dependent polycrystals. Acta Metall 33:923–953
88. Sinha S, Pukenas A, Ghosh A, Singh A, Skrotzki W, Gurao NP (2017) Effect of initial orientation on twinning in commercially pure titanium. Phil Mag 97–10:775–797
89. Eghtesad A Knezevic M (2021) A full-field crystal plasticity model including the effects of precipitates: Application to monotonic, load reversal, and low-cycle fatigue behavior of Inconel 718. Materials Science and Engineering A 803: 140478.
90. Savage DJ, Beyerlein IJ, Knezevic M (2017) Coupled texture and non-Schmid effects on yield surfaces of body-centered cubic polycrystals predicted by a crystal plasticity finite element approach. Int J Solids Struct 109:22–32
91. Alleman C, Ghosh S, Luscher DJ, Bronkhorst CA (2014) Evaluating the effects of loading parameters on single-crystal slip in tantalum using molecular mechanics. Phil Mag 94–1:92–116
92. Hama T, Suzuki T, Hatakeyama S, Fujimoto H, Takuda H (2018) Role of twinning on the stress and strain behaviors during reverse loading in rolled magnesium alloy sheets. Mater Sci Eng, A 725:8–18
93. Oliveira MC, Alves JL, Chaparro BM, Menezes LF (2007) Study on the influence of work-hardening modeling in springback prediction. Int J Plast 23:516–543
94. Hama T, Tanaka Y, Uratani M, Takuda H (2016) Deformation behavior upon two-step loading in a magnesium alloy sheet. Int J Plast 82:283–304
95. Hatakeyama S (2018) Crystal plasticity analysis of two-step deformation behavior in commercially pure titanium Grade 1 and Grade 2 sheets. Master thesis, Kyoto University.